Precambrian Research 388 (2023) 107018

Contents lists available at ScienceDirect

Precambrian Research

journal homepage: www.elsevier.com/locate/precamres

Multi-stage alteration at Nifty copper deposit resolved via accessory mineral dating and trace elements

Bruno V. Ribeiro [a,*], Christopher L. Kirkland [a], Michael I.H. Hartnady [a], Erin L. Martin [b,c], Emily West [b], Paul Polito [b]

[a] Timescales of Mineral Systems Group, School of Earth and Planetary Sciences, Curtin University, Bentley, WA 6102, Australia
[b] IGO Ltd, PO Box 496, South Perth, WA 6951, Australia
[c] Isotopia Laboratory, School of Earth, Atmosphere and Environment, Monash University, Clayton, Victoria 3800, Australia

A B S T R A C T

The sediment hosted Nifty prospect is one of the most prominent Cu deposits in the Neoproterozoic Paterson Province, which girdles the eastern margin of the Archean Pilbara Craton in Western Australia. The timing of mineralization at Nifty has proved challenging to constrain despite several attempts to date it using a range of isotopic methods, including muscovite $^{40}Ar/^{39}Ar$ (total fusion) and solution ICP-MS apatite U–Pb geochronology. The region preserves a protracted and complex geological history, with potential for several generations of fluid flow/mineralisation, which necessitates a texturally-controlled geochronology approach. Here, we report in situ apatite and monazite U–Pb isotopes complemented with trace elements from both mineralized veins and matrix of the sedimentary host-rock collected via laser ablation split stream inductively coupled plasma mass spectrometry (LASS-ICP-MS). Apatite grains from pyrite- and quartz-bearing veins are enriched in middle rare earth elements (MREE) with prominent convex-upward chondrite-normalized REE profiles. This chemical signature is similar to hydrothermal apatite from the Olympic Dam high-grade bornite Cu deposit, commonly associated with MREE-enriched, lower salinity fluids, and alkaline pH conditions capable of mobilizing Cu. Hydrothermal apatite from pyrite-bearing veins associated with euhedral, concentrically zoned pyrite yields lower intercept ages of ca 810 Ma, whereas hydrothermal apatite from quartz-pyrite veins associated with pyrite replacement microstructures have variable apparent ages. Monazite grains on the margins of pyrite-bearing veins (along micro-cracks) and monazite associated with chalcopyrite in veinlets yield a weighted mean $^{238}U/^{206}Pb$ age of ca 640 Ma. These results necessitate at least two distinct hydrothermal/fluid flow events related to the formation of the Nifty Cu deposit, with the former being temporally associated with ca 830 Ma mafic intrusions. Evidence for the latter hydrothermal event is cryptic, being highly localised at a grain scale, but is broadly coeval with ca 640 Ma granitic magmatism linked to Cu–Au mineralization elsewhere in the Paterson Orogen (e.g., Telfer & Winu deposits).

1. Introduction

Apatite is a Ca-phosphate present in various rock types, that crystallizes under a wide pressure–temperature-fluid conditions and is an important repository for uranium (U) and other trace elements (e.g., rare earth elements, Sr, Y). Its diverse chemistry means it has the potential to record various petrogenetic processes (Belousova et al., 2001; Chew and Spikings, 2015; Chu et al., 2009; Dempster et al., 2003; Faleiros et al., 2022; Harlov, 2015; Kirkland et al., 2018; Miles et al., 2014; Piccoli and Candela, 2019; Spear and Pyle, 2019; Watson and Green, 1981). Specifically, these characteristics means apatite is an important tool for mineral exploration given its ability to track fluid characteristics, based on trace element and halogen (Cl, F) composition, and date ore genesis using its U–Pb isotopic composition (Belousova et al., 2002; Cao et al., 2012; Chen et al., 2019; Chew et al., 2011; Chew and Spikings, 2015; Corfu and Stone, 1998; Krneta et al., 2017; Mao et al., 2016; Pan et al., 2016; van Daele et al., 2020; Zafar et al., 2020). Monazite [(Ce,La,Th)PO_4] is another useful phosphate mineral which grows under different petrogenetic conditions to apatite, typically when the REE cargo of fluids, especially Th, is elevated due to metamorphic reactions (Engi, 2018; Larson et al., 2022; Spear and Pyle, 2019; Zhu and O'Nions, 1999). Monazite can retain chemical domains, representing successive growth phases or alteration stages, as volatiles are liberated by tectonic and/or (hydro)thermal events (e.g., Weinberg et al., 2020). frequently recrystallizes in part or entirety when fluids are present via coupled substitution process $(2(Y + REE)^{3+} + \rightleftharpoons Th^{4+} + Ca^{2+})$ (Hetherington et al., 2010; Poitrasson et al., 1996; Williams et al., 2011). This process leaves the P–O framework of the monazite crystal intact, but variably purges the crystal of its radiogenic-Pb cargo, hence retaining a (variably) high-fidelity temporal record of fluid-mineral interaction. Thus, monazite may provide a complementary U–Pb chronometer to apatite (e.g., Prent et al., 2020), expanding the compositional environment across which petrogenetic processes can be tracked.

The Nifty deposit is one of the most significant Cu ore deposits of the

* Corresponding author.
E-mail address: bruno.vieiraribeiro@curtin.edu.au (B.V. Ribeiro).

https://doi.org/10.1016/j.precamres.2023.107018
Received 1 November 2022; Received in revised form 17 February 2023; Accepted 26 February 2023
Available online 7 March 2023

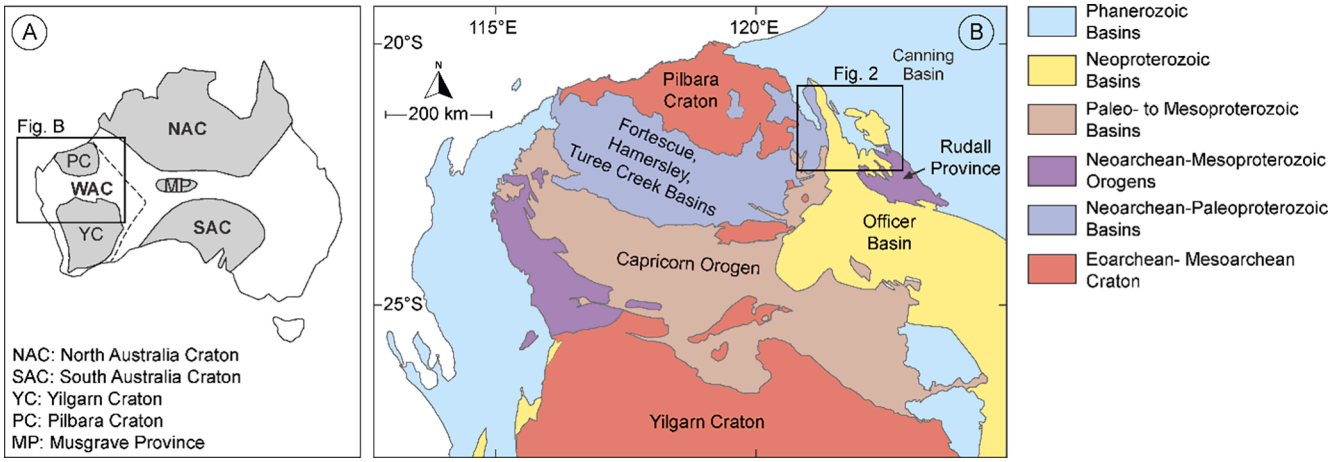

Fig. 1. A) Simplified tectonic framework of Australia highlighting the cratonic areas and the study area; B) Geological provinces of northern Western Australia.

Neoproterozoic Paterson Province which girdles the eastern margin of the Archean Pilbara Craton in Western Australia (Fig. 1A, B). The timing of this sedimentary-hosted stratiform Cu deposit has been contentious and challenging to decipher (Anderson et al., 2002, 2001; Huston et al., 2020). $^{40}Ar/^{39}Ar$ ages of mica linked to alteration were suggested to reflect deposit formation at ca 717 Ma (Anderson et al., 2001). In contrast, Huston et al. (2020) suggested an age interval spanning 850–800 Ma for ore genesis based on complex hydrothermal apatite U–Pb–Nd data collected via solution-mode ICP–MS. In this study, we investigate the timing of mineralization at Nifty using in situ apatite and monazite U–Pb geochronology and trace element data collected via laser ablation split stream inductively coupled plasma mass spectrometer (LASS-ICP-MS). The use of LASS-ICP-MS offers the ability to collect in situ isotopic and trace element data from sample volumes that can be screened via a range of imaging techniques for homogeneity with analyses placed in the context of their mineral-ore textural relationship.

2. Geological setting

2.1. The Paterson Orogen

The Paterson Orogen (Fig. 2) is a 2000 km long Paleoproterozoic-Neoproterozoic orogenic belt that extends from northern Western Australia to north-west South Australia (Bagas, 2004; Williams and Myers, 1990). It is the only exposed Proterozoic orogenic belt between the West and North Australian Cratons and is interpreted to record events related to their collision, during the formation of the early Australian continent (Bagas, 2004; Betts et al., 2015; Gardiner et al., 2018; Lu et al., 2022; Myers et al., 1996). The north-western area of the orogen is exposed along the eastern margin of the Archean Pilbara Craton (Ferguson et al., 2005; Williams and Myers, 1990). The Paterson Orogen is bordered to the north by the Permian Canning Basin, to the south by the Neoproterozoic Canning Basin, and to the east by the Proterozoic Canning Basin (Fig. 1) (Anderson et al., 2001; Williams and Bagas, 1999).

The southern exposure of the Paterson Orogen is subdivided into the Paleoproterozoic-Mesoproterozoic Rudall Complex and Neoproterozoic Yeneena and Officer basins (Ferguson et al., 2005; Williams and Myers, 1990). The Rudall Complex consists of metamorphosed igneous and sedimentary rocks that are unconformably overlain by the Yeneena Supergroup of the Yeneena Basin and Tarcunyah Group of the Yeneena or Officer Basin (Williams and Bagas, 1999). The Yeneena Supergroup is comprised of the Lamil and Throssel Range Groups (Bagas, 2004). The Throssell Range Group is a sandstone-shale-carbonate succession comprised of the Coolbro Sandstone, the Broadhurst Formation, and the Isdell Formation (Bagas, 2004; Ferguson et al., 2005). The Broadhurst Formation conformably overlies the Coolbro Sandstone and is dominated by carbonaceous shales and siltstones with interbedded sandstones and dolostones (Anderson et al., 2001; Bagas, 2004; Ferguson et al., 2005). The lower Broadhurst Formation is interpreted to reflect pelagic deposition following rapid basin subsidence, transitioning to a subtidal, low-energy shelf environment (Anderson et al., 2001). Detrital zircon grains from the Coolbro Sandstone provide a maximum deposition age of the Broadhurst Formation of ca 910 Ma (Huston et al., 2020; Nelson, 2002).

Three major orogenic events have deformed and metamorphosed the rocks in the Paterson Orogen, namely the Yapungku, Miles, and Paterson orogenies (Fig. 2) (Anderson et al., 2001; Bagas and Smithies, 1998; Hickman and Clarke, 1994; Smithies and Bagas, 1997). The 1790–1760 Ma Yapungku Orogeny has been regarded by some to reflect the amalgamation of the West and North Australian craton in an event that predates the Yeneena Supergroup (Cawood and Korsch, 2008). This event is characterized by a regional metamorphic foliation and isoclinal folding in the Rudall Complex under upper-amphibolite to lower granulite facies conditions (Bagas, 2004; Clarke, 1991; Hickman and Bagas, 1999; Payne et al., 2021). A magmatic event at ca 1310–1286 Ma (Camel Suite) represents localised potassic magmatism associated with a medium- to high-pressure metamorphic event (the Parnngurr Orogeny) (Gardiner et al., 2018). The tectonic setting for this magmatic suite is not currently well understood but Gardiner et al. (2018) highlighted it may reflect extension, possibly orogenic collapse or back-arc development following accretion. This event may represent the youngest possible timing for the amalgamation of West Australian Craton with the North Australian Craton. The Neoproterozoic Miles Orogeny (ca 680–630 Ma; Durocher et al., 2003) affected both the Rudall Complex and Yeneena Supergroup, which developed northwest-trending folds and thrusts with similar orientation to structures generated during the Yapungku Orogeny, but at lower metamorphic grade (typically greenschist facies) (Bagas, 2004; Gardiner et al., 2018). Following the Miles orogeny and slightly proceeding or contemporaneous with the subsequent Paterson orogeny, voluminous oxidized and reduced granites were emplaced throughout the belt. The granites range in age from ca. 650–630 Ma and are associated with the world-class Telfer Au-Cu deposit (Anderson et al., 2001) and the Cu-Au Havieron deposit (Duuring et al., 2022). The Neoproterozoic Paterson Orogeny (580–530 Ma; Payne et al., 2021) is interpreted to have involved transpression and dextral strike-slip movement on major northwest-trending faults, likely in intracratonic setting (Bagas, 2004; Gardiner et al., 2018) however, some authors have proposed a subduction driven model for the orogen (Martin et al., 2017).

Numerous base metal deposits and prospects have been discovered in the Yeneena Basin (Fig. 2) (Duuring et al., 2022; Ferguson et al., 2005), including the Telfer Au-Cu deposit hosted in the Lamil Group, and the

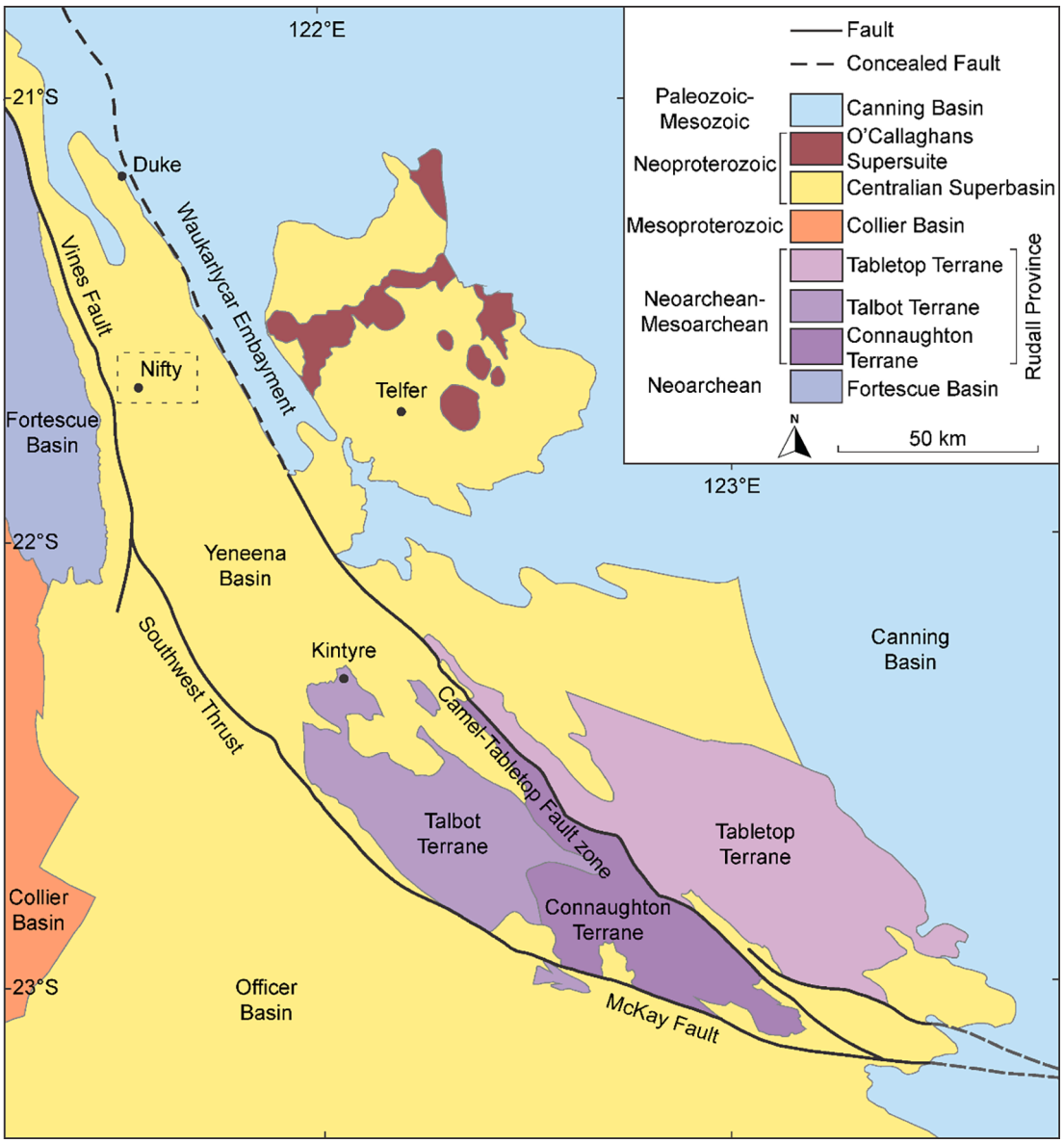

Fig. 2. Simplified geological map of the Neoproterozoic Paterson Orogen located at the eastern margin of the Pilbara Craton (simplified from Gardiner et al., 2018). The dashed-line rectangle locates the Nifty deposit.

Nifty Cu deposit hosted in the Broadhurst Formation (Anderson et al., 2001). Prospects proximal to Nifty also hosted by the Broadhurst Formation include the Rainbow Cu, Warrabarty Pb-Zn, and Maroochydore Cu prospects (Anderson et al., 2001). Recent discoveries of Cu-Au mineralization in the northern Paterson Orogen at Obelisk, Winu and Havieron highlight the potential of further mineralization in the orogen (Duuring et al., 2022).

2.2. Nifty Cu deposit

The Nifty deposit (Fig. 2) is hosted within the carbonaceous-dolomitic shale-dominated Broadhurst Formation (Anderson et al., 2001). The deposit is structurally controlled, with mineralisation typically forming stratiform lenses within the keel of a west-north-west trending open syncline (Anderson et al., 2001; Huston et al., 2020; Maidment et al., 2017). The deposit is subdivided into four stratigraphic members: footwall beds, the Nifty member, the pyrite marker bed, and hanging wall beds (Anderson et al., 2001). Ore mineralisation is hosted in the Nifty member, predominantly consisting of interbedded carbonaceous and chloritic shales and dolomitic mudstone (Anderson et al., 2001). The primary ore zone is overprinted by quartz-dolomite alteration, accompanied by apatite and carbonaceous matter (Anderson et al., 2001; Huston et al., 2020). The dominant sulphide mineralisation consists of chalcopyrite and pyrite, with minor sphalerite, galena and uranium-oxide present (Ferguson et al., 2005; Huston et al., 2020). Secondary copper mineralisation at Nifty occurs as supergene carbonate-hosted oxide and chalcocite mineralisation, and as remobilised shale-hosted mineralisation including malachite and azurite (Anderson et al., 2001; Ferguson et al., 2005; Maidment et al., 2017).

2.3. Samples of interest

Samples were recovered from diamond drill core NUG0399 at 101.7 m, 104.05 m, and 104.10 m depth, which crosscut the orebody close to the syncline axis, sampling the footwall bed of the deposit. The drill hole collar was located about 600 m from the centre of the Nifty open pit (latitude −21.664300 and longitude 121.575499). The three samples are shales of the Broadhurst Formation with quartz-bearing fine-grained

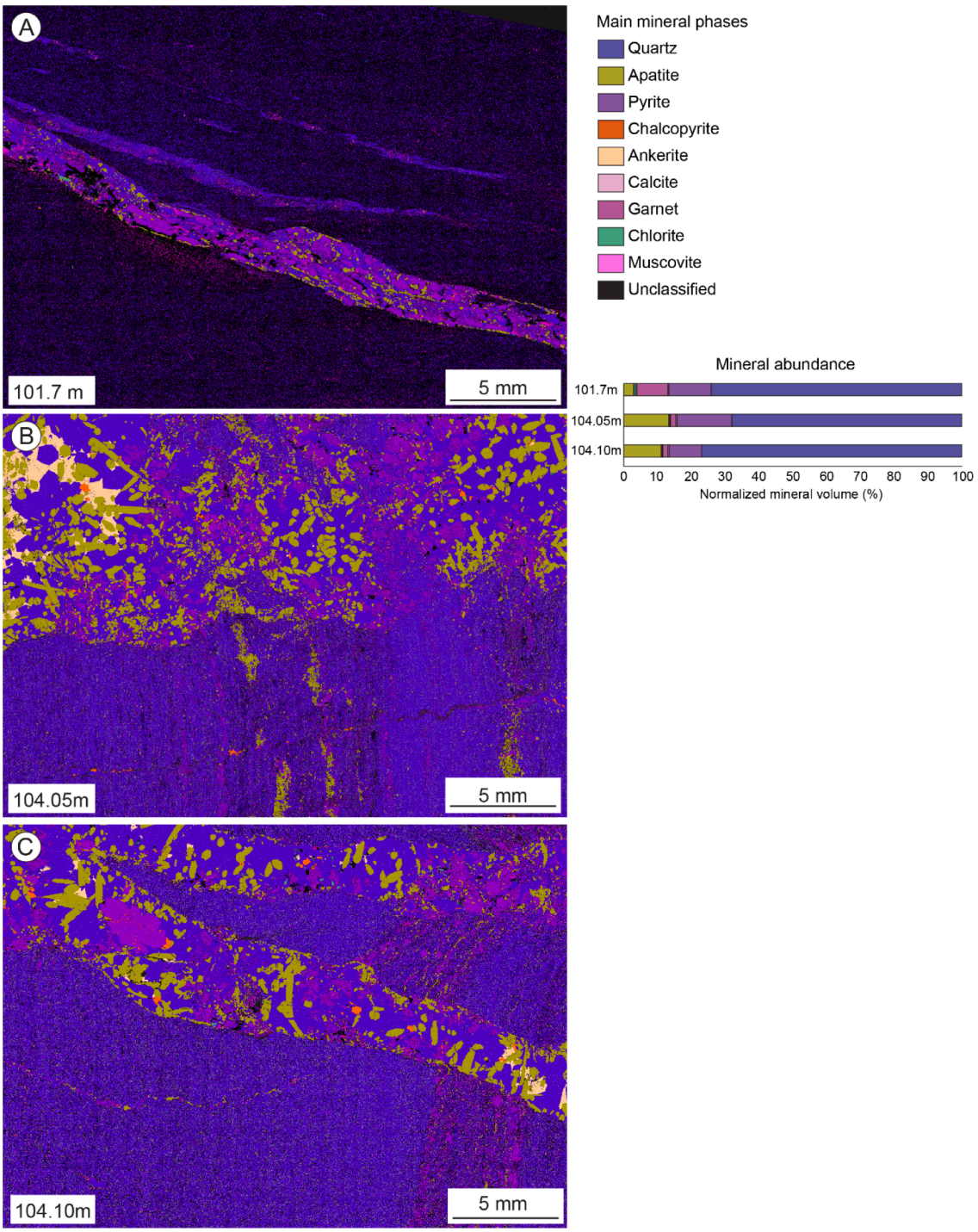

Fig. 3. Mineral assemblages and textures of the studied samples collected from different depths along the drill core. Sample number associated depth is located in the lower left corner of each photomicrograph. All mineralogical classification was performed using the TIMA software internal library.

mica matrix containing disseminated pyrite, apatite, chalcopyrite, and fine-grained muscovite and garnet along incipient planar bedding. Primary sedimentary layering is crosscut by apatite-pyrite-quartz (±chalcopyrite and monazite) veins and veinlets (i.e., narrow veins). The veins have fine-grained apatite in the margins (laminated zones) with coarse-grained apatite in the core (fibrous zone), variably oriented with respect to the vein boundaries (Fig. 3). These structures are consistent with antitaxial vein growth (Cox, 1987). The samples 101.7 m, 104.05 m, and 104.10 m were selected for in situ apatite and monazite U–Pb–trace element via LASS-ICP-MS.

3. Methods

In situ U–Pb–trace element analysis was performed on polished thin sections via LASS-ICP-MS at the John de Laeter Centre, Curtin University. Prior to isotopic analysis, the thin sections were scanned with TIMA (TESCAN integrated mineral analyzer) at the Microscopy and Microanalysis Facility of the John de Laeter Centre, Curtin University, to characterize the mineral assemblage of all samples. TIMA mapping was carried out with an accelerating voltage of 25 kV, a beam intensity of 19, probe current of 6.74–7.01nA, spot size of 67–90 nm, and nominal working distance of 15 mm. A pure Mn standard was used for EDS

spectra standardisation. Backscatter electrons (BSE) and energy-dispersive x-ray spectroscopy (EDS) analyses were referenced to a mineral library for automatic mineral classification.

3.1. U–Pb–trace element

The analytical setup includes a RESOLution SE excimer laser equipped with a Laurin Technic S155 cell connected to an Agilent 8900 QQQ ICP-MS for U–Pb measurements and to an Agilent 7900x Q ICP-MS for trace element measurements. Apatite analysis was conducted with a 50 μm spot size, 5 Hz repetition rate and laser energy of 3.2 $J.cm^{-2}$ measured above the laser cell. The sample cell was flushed with ultra-high purity He (320 $ml.min^{-1}$) and N_2 (1.2 $ml.min^{-1}$), both of which were passed through an inline Hg trap. Each analysis consisted of 30 s of baseline acquisition followed by 40 s of sample data acquisition and another 15 s of baseline counting. Unknowns were bracketed by a suite of reference glasses and apatite. Madagascar apatite (474 ± 1 Ma; Thomson et al., 2012) was employed as primary reference material for U–Pb, which yielded a weighted $^{238}U/^{206}Pb$ age of 474 ± 4 Ma (MSWD = 0.4, N = 18). McClure Mountain (Schoene and Bowring, 2006), FC-Duluth (Schmitz et al., 2003; Thomson et al., 2012) and Otter Lake (Barfod et al., 2005; Chew et al., 2011) apatite was employed as secondary reference material and treated as unknown. McClure Mountain apatite yields an unanchored regression lower intercept age of 517 ± 11 Ma (MSWD = 1.4, N = 17) and the FC-Duluth apatite yields an unanchored regression lower intercept age of 1057 ± 28 Ma (MSWD = 1.8, N = 18), in agreement with expected U–Pb ages. Otter Lake apatite yields an overdispersed, unanchored regression lower intercept age of 855 ± 44 Ma (MSWD = 4.3, N = 18), indicating minor grain-scale isotopic heterogeneities as previously observed (Thompson et al., 2016).

Monazite analysis was conducted with a 10 μm spot size, 4 Hz repetition rate and laser energy of 2.3 $J.cm^{-2}$ measured above the laser cell. The sample cell was flushed with ultrahigh purity He (320 $ml.min^{-1}$) and N_2 (1.2 $ml.min^{-1}$), both of which were passed through an inline Hg trap. Each analysis consisted of 30 s of baseline acquisition followed by 15 s of sample data acquisition and another 15 s of baseline counting. Unknowns were bracketed by a suite of reference glasses and monazite. Monazite 44,069 (430 ± 1 Ma; Aleinikoff et al., 2006) was employed as primary reference material for U–Pb, yielding a weighted mean $^{238}U/^{206}Pb$ age of 423 ± 3 Ma (MSWD = 0.7, N = 15). Stern (Horstwood et al., 2016) and Trebilcock monazite (Tomascak et al., 1996) were employed as secondary reference material and treated as unknowns. The secondary monazite reference material yielded the following weighted mean $^{238}U/^{206}Pb$ ages: 506 ± 3 Ma (Stern, MSWD = 0.9, N = 15), 275 ± 2 Ma (Trebilcock, MSWD = 0.4, N = 16). Data reduction was performed in Iolite4 (Paton et al., 2011) using the 'VizualAge UComPbine' data reduction scheme (Chew et al., 2014) for apatite and the built-in 'U-Pb Geochronology' data reduction scheme for monazite U–Pb isotopic data with an exponential with linear equation to correct for downhole isotopic fractionation. U–Pb ages were calculated using IsoplotR (Vermeesch, 2018), with ages and uncertainties being presented at the 2 σ confidence level. Apatite and monazite ^{207}Pb-corrected ages were calculated using Isoplot (Ludwig, 1991) considering a fixed $^{207}Pb/^{206}Pb_i$ isotopic ratio based on Stacey and Kramers (1975) terrestrial Pb evolution model, which were used to calculate Kernel density estimates were using IsoplotR (Vermeesch, 2018).

The international glass NIST610 was employed as primary reference material for trace element concentrations, and NIST612 was used as the secondary reference material and treated as an unknown to evaluate the reproducibility of the data. The results from the secondary standards indicate an accuracy of better than 5 % in comparison to the references values. ^{43}Ca and ^{140}Ce were used as internal standards for apatite and monazite, respectively, assuming an average stochiometric proportion. Trace element data reduction was performed using the built-in Trace Elements data reduction scheme in Iolite4. Trace element data from the reference materials employed in this study are consistent with published reference values (Chew et al., 2016; Yang et al., 2014). Apatite and monazite U–Pb–trace element data are presented in supplementary material S1 and S2, respectively.

4. Results

4.1. Petrographic summary

TIMA maps efficiently classify the mineral assemblages of a rock with complex deformation and/or alteration histories such as those presented in this study (e.g., Hrstka et al., 2018). All samples are predominantly composed of quartz + chalcopyrite + pyrite + apatite ± calcite ± ankerite ± garnet ± muscovite in different modal proportions (Fig. 3). Pyrite is the main sulfide phase and chalcopyrite is a minor phase in the studied samples. Sample 101.7 m has a fine-grained matrix composed of quartz + muscovite ± garnet crosscut by veins composed of quartz + pyrite + muscovite + apatite ± garnet ± chlorite (Fig. 3A). Samples 104.05 m and 104.10 m are similar, likely originating from the same stratigraphic layer, displaying a foliated matrix composed of fine-grained quartz + muscovite + garnet + apatite + granular pyrite crosscut by veins composed of quartz + pyrite + muscovite + apatite ± garnet ± chalcopyrite ± monazite (Fig. 3B-C).

4.2. Sulphide textures

We texturally classified three types of pyrite (Py_0, Py_1 and Py_2) based on reflected light photomicrographs and BSE images (Fig. 4). The matrix from all samples contains small pyrite grains (< 30 μm diameter), mostly rounded, typical of framboidal pyrite (Py_0; Fig. 4A–C) formed by the coalescence of individual pyrite grains as revealed by high-resolution BSE images (Fig. 4B, C; Sawlowicz, 1993). The pyrite-bearing vein from sample 101.7 m contains coarse-grained euhedral pyrite grains (Py_1). Many of these pyrite grains exhibit concentric zoning, visible in reflected light photomicrographs (Fig. 4D) and BSE images (Fig. 4E), containing small chalcopyrite inclusions. Although the zoning may represent trace element variations in Py_1, no trace element zoning was observed in the EDS elemental maps (Fig. 4F) likely due to the low sensitivity of the detectors. Alternative high-resolution mapping techniques such as laser ablation mapping is required to resolve the meaning of the concentric zoning of Py_1. Quartz-bearing veins from samples 104.05 m and 104.10 m display evidence of pyrite overgrowth textures (Fig. 4G, H). This texture indicates that Py_1 was modified by anhedral, porous and quartz-rich pyrite (Py_2), likely associated with secondary hydrothermal processes. We observed a Co element enrichment in the boundary between euhedral Py_1 and porous quartz-rich Py_2 in the elemental map collected from EDS analysis (Fig. 4I). Chalcopyrite is low abundant is the quartz-bearing veins (<5 %), commonly occurring as dispersed single grains. Yet, it is more frequent in microcracks along the vein walls and in veinlets crosscutting the sample, commonly associated with monazite.

4.3. Apatite textures

Apatite is present in both the host-rock matrix and veins in all samples. Sample 101.7 m has a low abundance of anhedral fine-grained apatite randomly dispersed in the matrix, and anhedral inequigranular apatite grains in the veins. Vein apatite are concentrated along the vein-matrix boundary, and in the pyrite-quartz boundaries commonly associated with garnet (Fig. 5A, D). Samples 105.05 m and 104.10 m also have anhedral to subhedral fine-grained apatite grains randomly dispersed in the matrix, but often contain apatite agglomerations parallel to the sedimentary layering, that are associated with pyrite, quartz, garnet, muscovite, and rare chlorite (Fig. 5B–C). The vein apatite grains from samples 104.05 m and 104.10 m are coarse-grained (up to 500 μm), euhedral to subhedral prismatic crystals, which are variably oriented with respect to the vein boundaries (Fig. 5B).

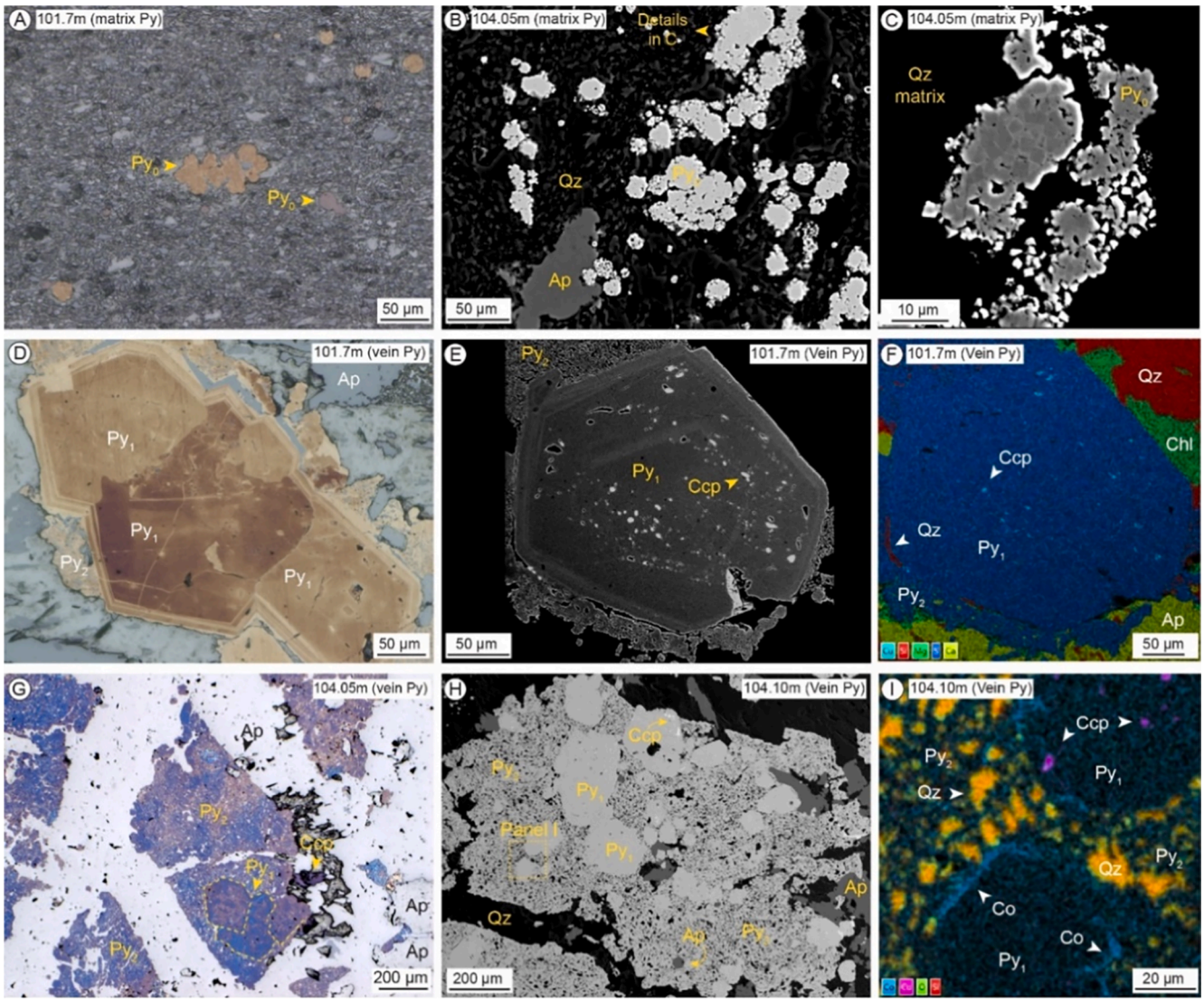

Fig. 4. Pyrite textures from samples 101.7 m, 104.05 m and 104.10 m. A) Reflected light photomicrograph of framboid pyrite (Py_0) from sample 101.7 m; B-C) Electron backscatter images of framboidal pyrite (Py_0) from sample 104.05 m; D) Reflected light photomicrograph of euhedral pyrite (Py_1) displaying concentric zoning from sample 101.7 m; E) Electron backscatter image of euhedral pyrite (Py_1) from sample 101.7 m; E) Elemental map of euhedral pyrite (Py_1) from energy Dispersive Spectroscopy (EDS) analysis; G) Reflected light photomicrograph of pyrite overgrowth textures from sample 104.05 m; H) Electron backscatter images of pyrite overgrowth textures from sample 104.10 m; I) Elemental map of pyrite overgrowth textures from sample 104.10 m from EDS analysis. Mineral abbreviations follow Whitney and Evans (2010).

4.4. Monazite textures

Monazite grains from all samples are generally very fine-grained (<15 µm), anhedral and commonly developed along the interface between the larger quartz-pyrite veins and the host-rock matrix (Fig. 5A, D) and also in thinner chalcopyrite-bearing veinlets that crosscut sedimentary layering (Fig. 5E, F). In sample 101.7 m, the monazite grains define a trail along the matrix-vein interface in association with fine-grained pyrite, commonly filling microcracks (Fig. 5D). Monazite grains from samples 104.05 m and 104.10 m are present in fine veins mainly composed of quartz, chalcopyrite, pyrite and ± garnet. In these samples, the monazite grains are associated with chalcopyrite resembling a corona texture (Fig. 5F), typical of hydrothermal monazite from ore systems (e.g., de Melo et al., 2019; Milton et al., 2017).

4.5. Apatite U–Pb–trace element

We collected a total of 40 U–Pb analyses from vein apatite grains in sample 101.7 m. The data define a discordia array in the Tera-Wasserburg diagram indicating a lower intercept age of 809 ± 12 Ma (MSWD = 3.6) with an $^{207}Pb/^{206}Pb_i$ of 0.85 ± 0.02 (Fig. 6A). The elevated MSWD implies the scatter exceeds analytical uncertainties alone and may be attributed to minor radiogenic-Pb loss.

A total of 47 U–Pb measurements were collected from matrix apatite of sample 104.05 m, and 60 U–Pb measurements were collected from vein apatite grains. The matrix apatite U–Pb data define an over-dispersed discordia in the Tera-Wasserburg diagram suggesting a lower intercept age of 810 ± 5 Ma (MSWD = 5.6) with an $^{207}Pb/^{206}Pb_i$ of 0.84 ± 0.02. The MSWD implies scatter around the regression as a consequence of either or both radiogenic-Pb loss or recrystallization (Fig. 6B). The vein apatite U–Pb data also define a discordia with a more radiogenic $^{207}Pb/^{206}Pb_i$ ratio, yielding a younger lower intercept age of 775 ± 7 Ma (MSWD = 10) with an initial of $^{207}Pb/^{206}Pb_i$ 0.89 ± 0.03, identical to that predicted by the Stacey and Kramers (1975) terrestrial Pb evolution model for this age.

From sample 104.10 m, a total of 16 U–Pb measurements were collected from matrix apatite and 54 U–Pb measurements were collected from vein apatite grains. The matrix apatite dataset defines an

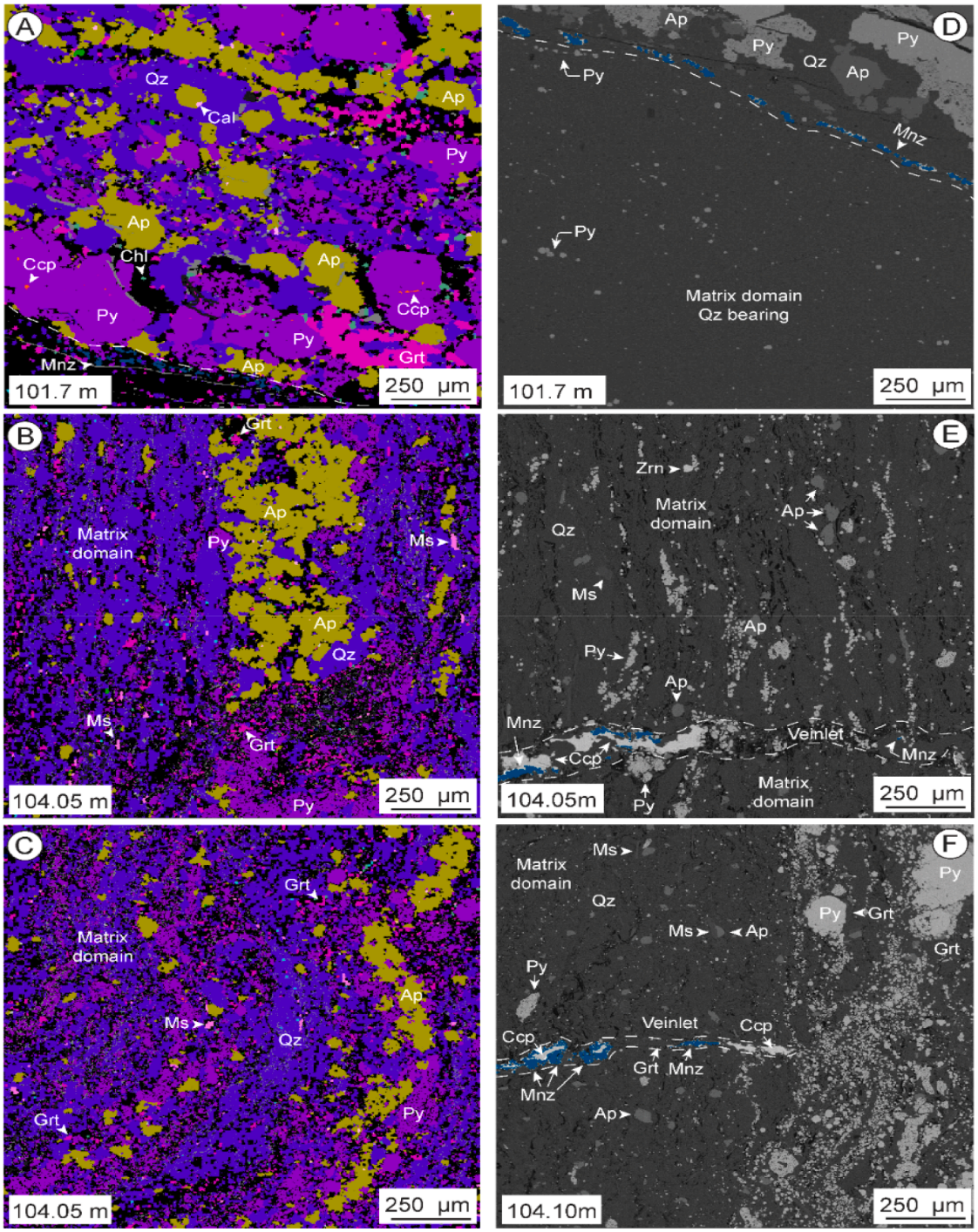

Fig. 5. Apatite and monazite textures from samples 101.7 m, 104.05 m and 104.10 m. A) Phase map from the vein texture of sample 101.7 m; B-C) Phase map of the matrix texture of samples 104.05 m and 104.10 m; D-F) Backscatter electron images focusing on the monazite textures along matrix-vein/veinlets boundaries from samples 101.7 m, 104.05 m and 104.10 m, respectively. Mineral abbreviations follow Whitney and Evans (2010).

overdispersed discordia between common and radiogenic components, suggesting a lower intercept age of 795 ± 17 Ma (MSWD = 5.3) with an $^{207}Pb/^{206}Pb_i$ of 0.86 ± 0.01 (Fig. 6C). The vein apatite U–Pb data define an overdispersed discordia in the Tera-Wasserburg diagram suggesting a lower intercept age of 747 ± 8 Ma (MSWD = 11) with an initial $^{207}Pb/^{206}Pb$ 0.95 ± 0.04. The dispersion on the mixing array is similar to the other samples implying post crystallization modification.

Chondrite-normalized REE patterns of the matrix apatite are similar across all three samples, suggesting they grew from the same fluid, or fluids of similar composition (Fig. 6D–F). Both matrix and vein apatite grains have a prominent convex shape with a dominance of medium-REE (MREE) over light-REE (LREE) in comparison to igneous apatite patterns (Belousova et al., 2001; O'Sullivan et al., 2020; Piccoli and Candela, 2019). Despite the predominance of convex chondrite-normalized REE patterns for most matrix and vein apatite grains, some matrix apatite grains from sample 104.10 m are distinct with a higher REE content (average of ~1060 ppm) and steeper REE patterns with average $(La/Yb)_N$ ratio of 2.2, diverging from the typical REE-depleted convex patterns with lower average $(La/Yb)_N$ ratio of 0.6.

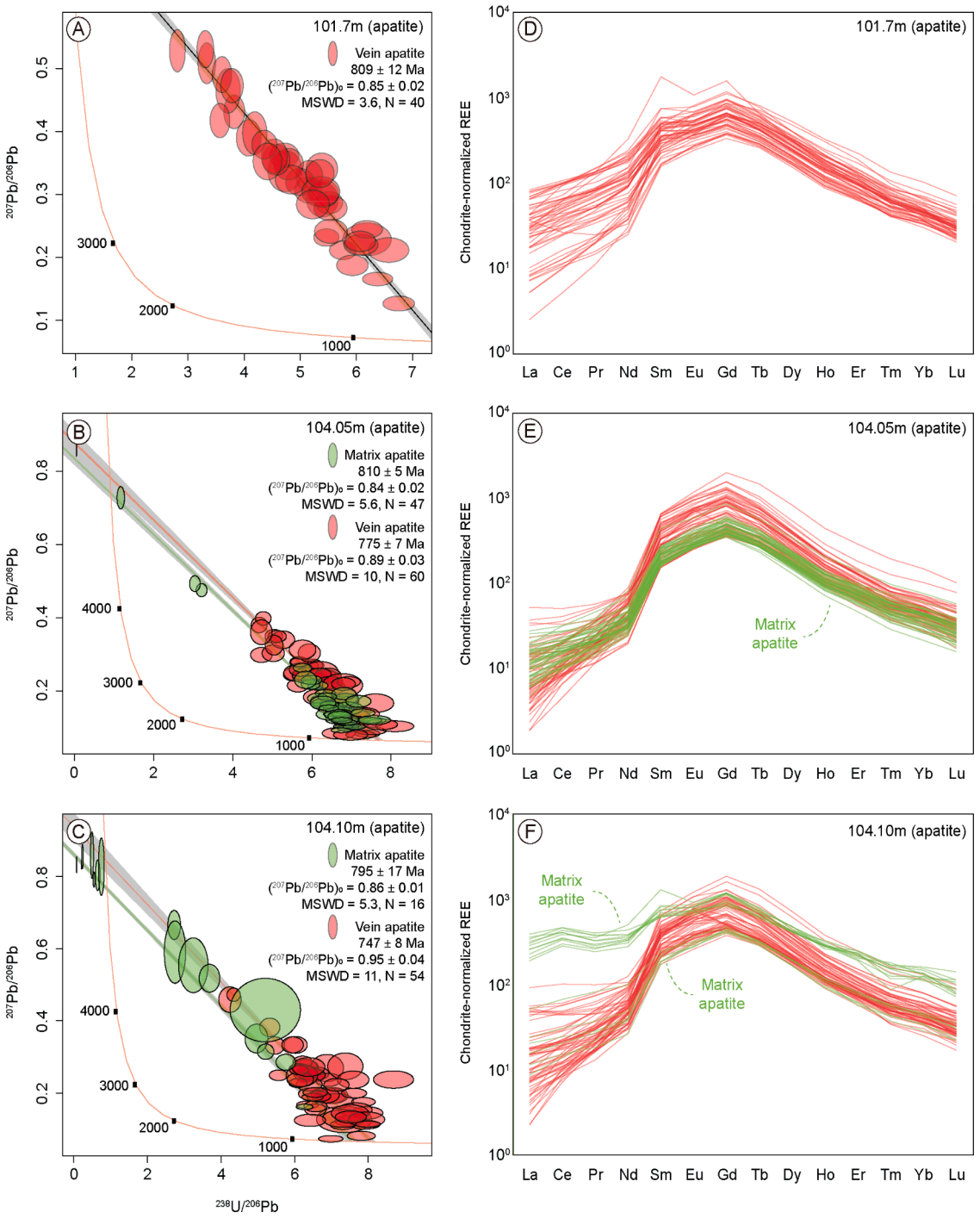

Fig. 6. A–C) Tera-Wasserburg diagram of apatite U–Pb data from samples 101.7 m, 104.05 m and 104.10 m, respectively. The U–Pb data is differentiated into matrix (green ellipsis) and vein apatite (red ellipsis) based on the TIMA maps. Ellipse uncertainties and errors are presented at 2 σ level of confidence. Tera-Wasserburg diagrams were calculated using IsoplotR (Vermeesch, 2018); D-F) apatite chondrite-normalized REE of samples 101.7 m, 104.05 m and 104.10 m. Rare earth element concentrations were normalized by the chondrite reference values from McDonough and Sun (1995). (For interpretation of the references to colour in this figure legend, the reader is referred to the web version of this article.)

4.6. 4.6. Monazite U–Pb–trace element

Sixteen monazite U–Pb measurements from sample 101.7 m were undertaken, which define a radiogenic/common-Pb mixing array yielding a lower intercept age of 648 ± 12 Ma (MSWD = 4.2) with an initial $^{207}Pb/^{206}Pb_i$ of 1.11 ± 0.10. (Fig. 7A). Although the results did not yield any concordant data, the lower intercept age is consistent with the ^{207}Pb-corrected weighted $^{238}U/^{206}Pb$ mean age of 643 ± 8 Ma (MSWD = 3.1), calculated using an $^{207}Pb/^{206}Pb_i$ as predicted by the Stacey and Kramers (1975) terrestrial Pb evolution model for Neoproterozoic crust (i.e., ~0.86 for 650 Ma). From sample 104.05 m, we collected 12 monazite U–Pb measurements, but the majority of the ratios are overdispersed with respect to a single radiogenic-common mixing line, implying various secondary modification processes. Three analyses yield a lower intercept age in the Tera-Wasserburg diagram of 675 ± 21 Ma (MSWD = 0.1) with a $^{207}Pb/^{206}Pb_i$ 1.40 ± 0.28 (Fig. 7B). Two concordant analysis yields a concordia age of 675 ± 21 Ma (MSWD = 0.1). Twenty-one monazite U–Pb analyses from sample 104.10 m were

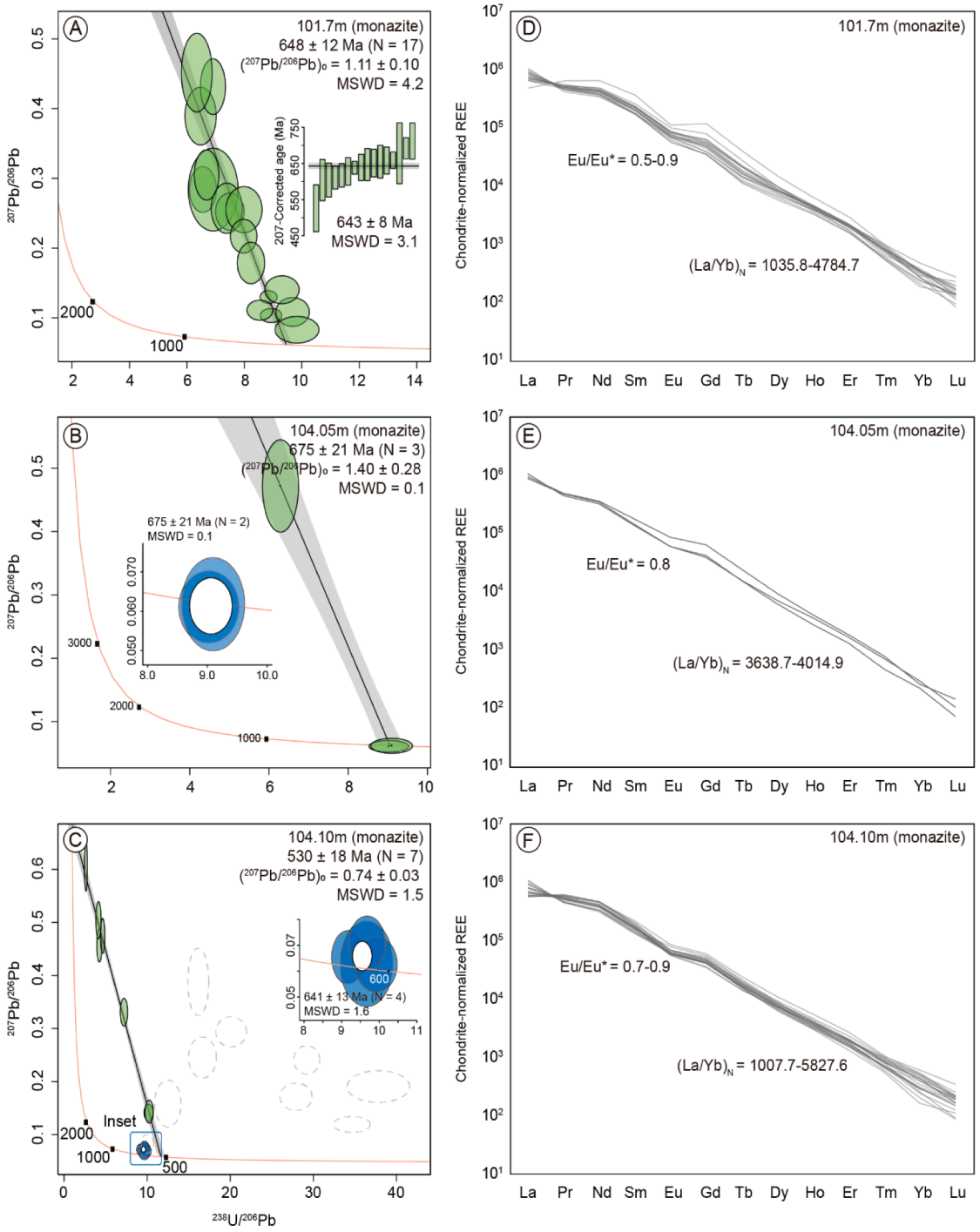

Fig. 7. Tera-Wasserburg diagrams of monazite U–Pb data (A–C) and chondrite-normalized REE (D-F) of samples 101.7 m, 104.05 m and 104.10 m. Ellipse uncertainties are 2 σ and errors are studentized at 95 % confidence with no common-Pb correction applied. Tera-Wasserburg diagrams were calculated using IsoplotR (Vermeesch, 2018). Rare earth element concentrations were normalized by the chondrite reference values from McDonough and Sun (1995).

performed. Seven spots define a discordia trend in the Tera-Wasserburg plot yielding a lower intercept age of 530 ± 18 Ma (MSWD = 1.5) with a $^{207}Pb/^{206}Pb_i$ of ~ 0.74 ± 0.03 (Fig. 7C). Four spots within a maximum ± 10 % ($^{207}Pb/^{235}U$ age/$^{206}Pb/^{238}U$ age) discordance threshold, yield a concordia age of 641 ± 13 Ma (MSWD = 1.6) (Fig. 7C, inset), defining the most concordant age component among the three samples.

The monazite chondrite-normalized REE patterns are similar across all three samples, displaying highly fractionated patterns with LREE dominance indicated by the high $(La/Yb)_N$ ratios and slightly negative E anomalies with Eu/Eu* varying from 0.5 to 0.9 (Fig. 7D-F). These patterns are consistent with hydrothermal monazite from ore deposits (Zhu and O'Nions, 1999).

5. Discussion

5.1. Significance of apatite and monazite trace element patterns

Apatite is known to display fractionated chondrite-normalized REE with $(La/Nd)_N$ ratios commonly higher than 1 and negative Eu anomalies due to usual co-crystallization with feldspar (Belousova et al., 2001;

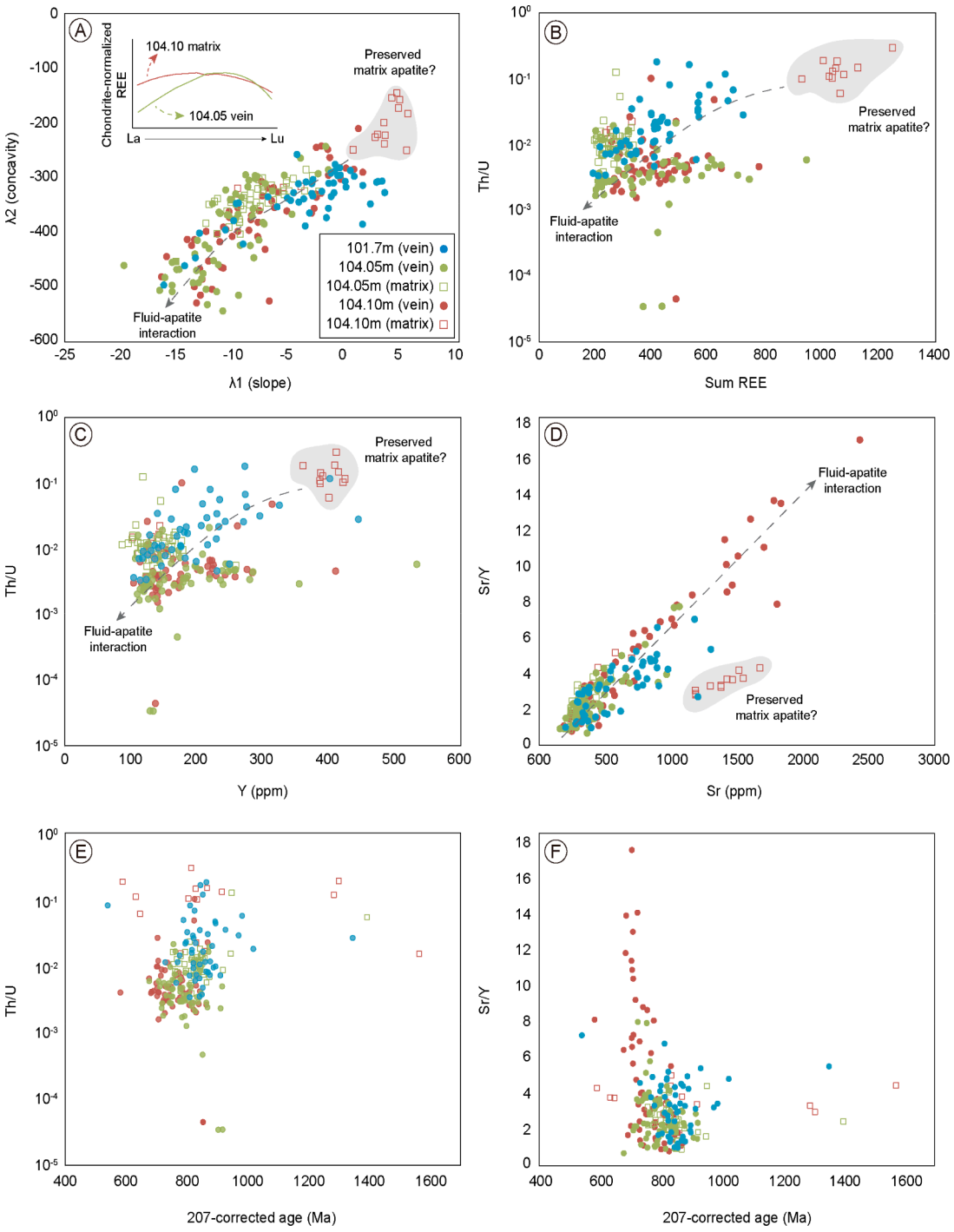

Fig. 8. Trace element diagrams based on the vein and matrix apatite data from samples 101.7 m, 104.05 m and 104.10 m. Filled circles represent vein apatite grains and hollow squares represent matrix apatite grains. Diagram (A) uses the lambda coefficient (λ_1 and λ_2) to mathematically represent the slope and the concavity of the chondrite-normalized REE patterns (see O'Neill, 2016 for details). The lambda coefficients were calculated using the online BLambdaR tool (Anenburg, 2020; Anenburg and Williams, 2022). The inset (A) demonstrates the slope and concavity increase towards lower λ_1 and λ_2 values, which is accompanied by a decrease in total REE (B), Th/U and Y (ppm) (C) and Sr and Sr/Y increase (D).

Cao et al., 2012; Long et al., 2023; O'Sullivan et al., 2020). These chemical characteristics can be preserved despite metamorphic overprinting, which might reset the age via thermally activated Pb volume diffusion in dry conditions (Cabrita et al., 2022; Ribeiro et al., 2022, 2020b). However, apatite trace element systematics are very susceptible to reactions with fluids, typically causing LREE, Th/U, and Y depletion accompanied by Sr increases (Harlov, 2015; Henrichs et al., 2019, 2018; Odlum et al., 2022; Odlum and Stockli, 2020; O'Sullivan et al., 2020; Ribeiro et al., 2022, 2020a). These characteristics highlight the key use of apatite geochemistry to track fluid-rock interaction (Belousova et al., 2002; Mao et al., 2016; Pan et al., 2016).

The vein apatite grains and the vast majority of the matrix apatite grains are LREE- and HREE-depleted resulting in convex chondrite-normalized REE patterns as demonstrated by the λ_1 (slope) and λ_2

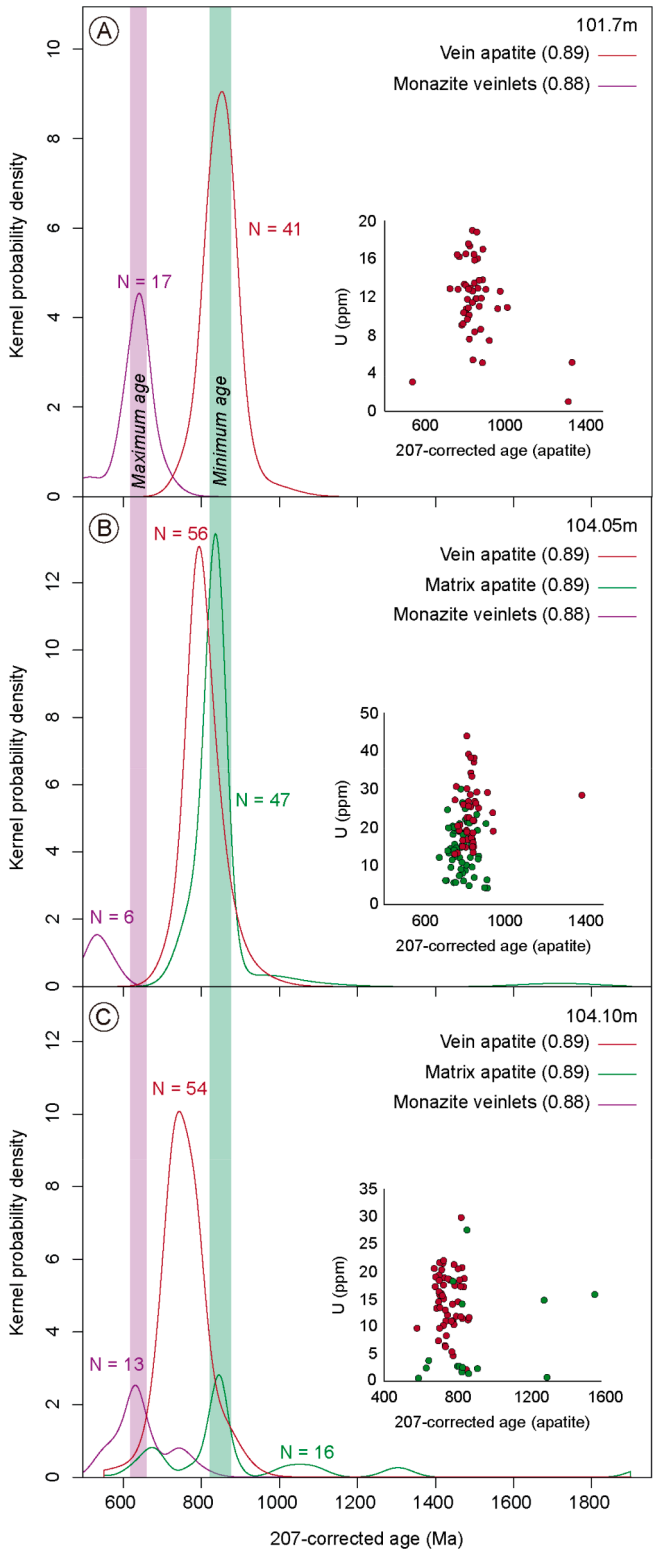

Fig. 9. Kernel density estimate diagrams of apatite and monazite 207-corrected ages (Ma). The initial $^{207}Pb/^{206}Pb$ was calculated using Stacey & Kramers (1975) and the values are presented in parenthesis in the top right of each diagram. The 207-corrected ages were calculated using initial $^{207}Pb/^{206}Pb$ of 0.88 (monazite; 650 Ma) and 0.89 (apatite; 810 Ma) consistent with the timespan constrained by the isochron and with galena Pb isotopic from the Nifty deposit (Anderson et al., 2002). Insets represent the correlation between 207-correct apatite ages vs. U (ppm). Red and green circles represent vein and matrix apatite grains. (For interpretation of the references to colour in this figure legend, the reader is referred to the web version of this article.)

(concavity) coefficients (Fig. 8A). The lambda parameter (λ_n) is a shape coefficient that mathematically describes the chondrite-normalized REE pattern with λ_1 and λ_2 describing the linear slope and quadratic curvature components, respectively (see O'Neill (2016) for details). The increase in slope (lower λ_1) and concavity (lower λ_2) is accompanied by a decrease in total REE content, Th/U, and Y, accompanied by the Sr concentration and Sr/Y increase (Fig. 8B–D). These apatite trace element characteristics are generally associated with hydrothermal environments and fluid-assisted recrystallization, with LREE and fluid-mobile Sr being transferred to REE-Sr enriched phases such as monazite, epidote, allanite, and micas or into the fluid itself (Harlov, 2015; Henrichs et al., 2019, 2018; Odlum and Stockli, 2020; Ribeiro et al., 2020a; Spear and Pyle, 2019). We note that 11 matrix apatite results from sample 104.10 m display higher total REE content, shallower slope (higher $\lambda 1$) and concavity (λ_2), associated with higher Y concentration and Th/U ratios (Fig. 8B, C). These apatite results also plot separately from the Sr vs. Sr/Y array defined by the majority of vein and matrix apatite grains (Fig. 8D). Given the sedimentary protolith of these rocks and the distinct characteristics of those 11 matrix apatite results from sample 104.10 m, it seems reasonable to interpret these grains as likely detrital apatite that were less affected by metasomatism, allowing them to partially preserve their primary trace element characteristics. Conversely, this mineral chemistry may represent an early syn-sedimentary carbonate fluorapatite (francolite), an authigenic mineral that precipitates from pore water during sedimentation (Mcarthur, 1985).

The apatite convex-shape of the REE-chondrite normalized profiles are similar to those from hydrothermal apatite from the Olympic Dam high-grade bornite (Cu_5FeS_4) deposit (Krneta et al., 2017). Numerical models based on oxygen fugacity, pH, salinity, ionic complex activity and temperature parameters have demonstrated that these MREE-enriched apatite with convex chondrite-normalized REE patterns are best associated with low saline and alkaline MREE-enriched fluids (Krneta et al., 2018). Such fluids have a higher capacity to mobilize Cu due to the transition from $EuCe_4^{-2}$ to EuO_2^{-2} (Brugger et al., 2008; Krneta et al., 2018), which may explain the predominance of pyrite (FeS_2) over chalcopyrite ($CuFeS_2$).

Monazite grains from all three samples are commonly found in the matrix-vein boundaries or fine veins associated with chalcopyrite, defining a "corona-like" texture (Fig. 4D–F). These monazite grains display highly fractionated chondrite-normalized REE patterns with weak negative Eu anomalies. These textural and chemical characteristics suggest hydrothermal origin, similar to monazite from other ore deposits worldwide (de Melo et al., 2019; Milton et al., 2017; Zhu and O'Nions, 1999). The strong HREE depletion may be caused by coeval garnet crystallization in the fluid source (see Fig. 4F), which has a higher HREE affinity than monazite (Larson et al., 2022; Zhu and O'Nions, 1999).

In summary, we conclude that the apatite vein and most of the apatite matrix were crystallized or re-equilibrated during hydrothermal events, likely with fluids of high pH and low salinity during an early-mid Tonian fluid event (ca 810 Ma) (Fig. 9). The apatite-chalcopyrite and apatite-pyrite petrographic association in these samples may indicate that the Cu-Fe mineralization was associated with the aforementioned fluid. The scarcity of monazite in larger veins and its dominant presence in thin veinlets and microcracks along the interface between large veins and host-rock matrix, implies that monazite developed as a minor late-stage hydrothermal mineral. The association between monazite and chalcopyrite in some veinlets (Fig. 4E, F) indicates this late-stage hydrothermal event may have also (re)mobilised Cu. We highlight that the samples from this study were sampled from a single drill core at Nifty and hence may not represent the entire deposit history. Thus, more studies and samples are required to investigate the extent of the features observed in this study throughout the deposit.

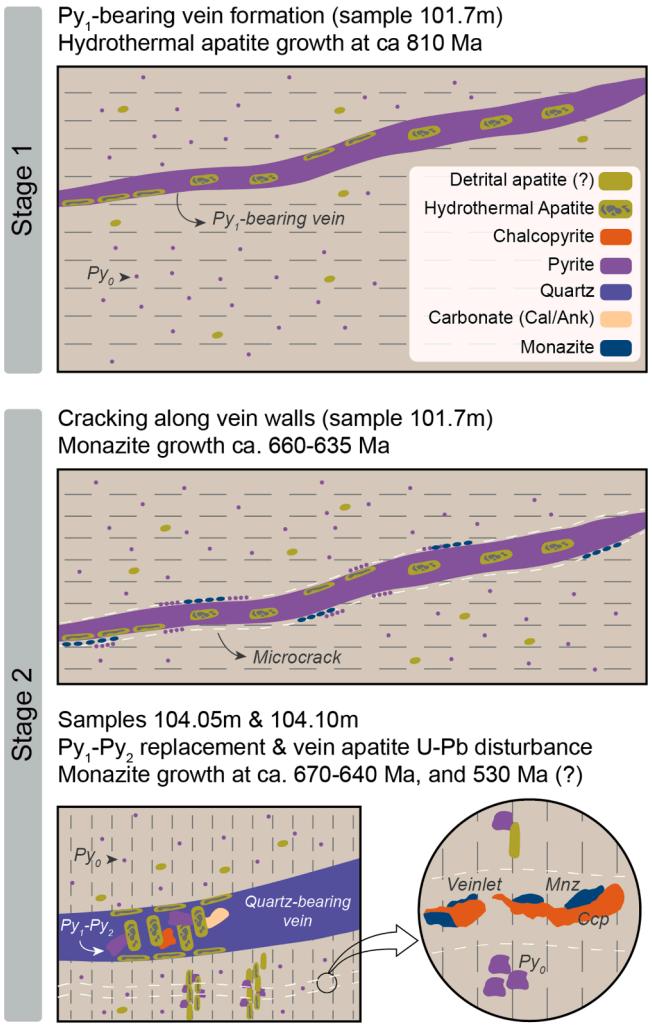

Figure 10

Fig. 10. Schematic evolution of the vein formation stages of the Nifty deposit based on apatite and monazite ages and pyrite microstructures.

5.2. Significance of apatite and monazite U–Pb ages

The apatite U–Pb isotopic results demonstrate age differences between matrix and vein apatite grains. Matrix apatite grains from samples 104.05 m and 11 matrix apatite grains from sample 104.10 m with distinct trace element characteristics (average ^{207}Pb-corrected of ca 825 Ma) indicate older ages spanning early-mid Tonian, whereas the vein apatite grains define a younger population of ca 780–750 Ma (Fig. 9). Apatite U–Pb results from sample 101.7 m are the least scattered, whereas the results from samples 104.05 m and 104.10 m are highly scattered indicating some modification to the U–Pb isotopic systematics occurred. The correlation between apatite Th/U and Sr/Y and ^{207}Pb-corrected ages (Fig. 8E, F) implies that fluid-assisted recrystallization is the dominant process resetting the apatite U–Pb system rather than volume diffusion alone (e.g., Harlov, 2015; Ribeiro et al., 2020a), modifying the trace element of most vein and matrix apatite during the Tonian-Cryogenian. The trace element similarity among all three samples suggests that most of the matrix apatite and the vein apatite grew from/or equilibrated with fluids of similar composition, if not the same fluid. Hence, based on the apatite data alone, it is unclear if the different apparent ages obtained from this mineral reflect real discrete hydrothermal and potentially mineralisation events, or are related to other, potentially more recent, partial secondary modification processes.

Monazite U–Pb data from samples 101.7 m and 104.10 m provide evidence for younger hydrothermal events around ca 670–640 Ma and ca 550–510 Ma. Yet, these hydrothermal events did not significantly modify the rock textures, in some places intragranular fluid flow through the rock mass during this event likely affected the apatite U–Pb isotopic system, causing the spread in apatite ages from ca 810 Ma to 750 Ma. This interpretation is well illustrated in the Kernel density estimate diagrams (Fig. 9). Matrix apatite grains from samples 104.05 m and 104.10 m define a maximum age of ca 850–800 Ma, whereas monazite grains from samples 101.7 m and 104.10 m define a minimum age of 670–640 Ma for the Nifty deposit (Fig. 9). Vein apatite from sample 101.7 m, however, preserves older ca 810–800 Ma ages, likely due to shielding by the vein fill from younger fluids that localised into the vein margins. This shielding potentially allowed the vein apatite from sample 101.7 m to maintain its isotopic cargo.

Since the vein apatite ^{207}Pb-corrected ages from sample 101.7 m match with the minimum age of ca 810 Ma from matrix apatite in samples 104.05 m and 104.10 m, we suggest these dates represent the best estimate for the age of vein formation. At that time, the matrix-hosted apatite grains underwent fluid-driven recrystallization affecting their primary U–Pb systematics and trace element composition. Given the similar trace element patterns and age similarity between the vein apatite and most of the matrix apatite, it is likely that most matrix-hosted apatite also crystallised during vein formation. However, some apatite in sample 104.10 m preserve apparently older ^{207}Pb-corrected U–Pb dates that are compositionally distinct, indicating they may represent detrital apatite grains or authigenic material that precipitated from pore water (francolite).

Previous studies on the Nifty deposit using solution ICP-MS apatite U–Pb geochronology also yielded variable isotopic results. Huston et al., (2020) used five small splits of apatite containing 4–20 grains from two samples for trace element measurements via solution-mode ICP-MS and another four splits containing 4–5 mg for solution-mode U–Pb isotopic measurements via multi-collector ICP-MS. The trace element results of Huston et al., (2020) show convex chondrite-normalized REE patterns similar to those in this study, however, the solution U–Pb results yielded variable U-Pb ratios with apparent ages spanning 850–600 Ma. In an attempt to calculate U–Pb and Pb–Pb ages, Huston et al. (2020) were forced into some difficult data filtering choices, such as excluding apparent outliers in small populations to calculate an age estimate. On the basis of their approach, apatite crystallization and ore formation was suggested to have occurred at 822 ± 23 Ma (MSWD = 1.5). The recalculation of the Pb–Pb ages using the complete apatite dataset yields a ^{207}Pb/^{204}Pb vs. ^{206}Pb/^{204}Pb isochron age of 908 ± 28 Ma (MSWD = 14), demonstrating significant variability in Pb isotopic ratios in that dataset. Although the age estimate of 822 ± 23 Ma from Huston et al. (2020) is consistent with the matrix apatite U–Pb age spanning 850–800 Ma determined via in situ LASS-ICP-MS in this study, the matrix and vein apatite age variability implies that the over-dispersed apatite U–Pb results from Huston et al. (2020) represent real variability due to mixing of matrix and vein apatite components, in addition to variability inherent to the apatite itself. Such mixtures would be inevitable given the intimate association of veins and matrix that would be all but impossible to separate using solution-based isotopic analysis methods.

5.3. Evolution model

We propose an evolution model for the vein formation of the Nifty deposit involving a minimum of two-stages based on the new apatite and monazite U–Pb–trace element and pyrite textures in this work (Fig. 10). Although this model may represent only a snapshot in the evolution of Nifty, it contributes to a more comprehensive understanding of this complex mineral system.

Stage 1 represents pyrite-bearing vein formation composed of euhedral pyrite (Py_1) + quartz + garnet + apatite ± chlorite and ± chalcopyrite (<1 %). The timing of stage 1 is constrained by

hydrothermal apatite crystallization during early to mid-Tonian (ca 850–800 Ma; Fig. 10), accompanied by fluid-assisted recrystallization of matrix apatite as observed in samples 104.05 m and 104.10 m (Fig. 9). Stage 2 represents a late-stage fluid percolation through quartz-bearing veins, cracks along the interface between the pyrite-bearing vein and host-rock matrix, and thin veins (veinlets) through the matrix. The timing of this stage is constrained by hydrothermal monazite crystallization at 670–640, with a potential later event at 550–510 Ma, associated with the formation of Py_1-Py_2 replacement textures and precipitation of chalcopyrite. These younger hydrothermal events may have enhanced recrystallization and partially reset apatite U–Pb systematics in the quartz-bearing veins of samples 104.05 m and 104.10 m, leading to greater apparent age dispersion (Fig. 6B-C and 9). The changes in vein mineralogy suggest a change in fluid composition from stage 1 to stage 2. We infer that fluids from stage 1 are more capable of dissolving and transporting Cu as inferred from the apatite geochemistry as discussed elsewhere (e.g., Krneta et al., 2018, 2017), hence the low abundance of Cu-bearing minerals such as chalcopyrite. The crystallization of Cu-bearing minerals texturally associated with monazite during stage 2 implies that Ediacaran-Cambrian hydrothermal events in the Paterson Orogen had favourable conditions to precipitate Cu-bearing minerals (Reed, 2006; Zhong et al., 2015).

5.4. Regional inferences

The Paterson Orogen hosts diverse mineralization, in addition to sediment-hosted Cu at Nifty, intrusion-related/orogenic Au–Cu is known from Telfer, vein and disseminated Cu–Au–Ag at Winu, unconformity-associated U at Kintyre, skarn W–Cu–Zn at O'Callaghans and Mississippi Valley-type Pb–Zn at Warrabarty deposits (Huston et al., 2020; Maidment et al., 2017). The tectonic setting and evolution of the Nifty deposit is in some respects poorly understood due to the complexity of the published geochronology on this deposit, in part a function of the type of minerals investigated (low U, high common Pb). Nifty lies within the Broadhurst Formation of the Yeneena Basin, a Neoproterozoic basin exposed on the northeastern margin of the West Australian Craton and deposited on extended crust of the Archean Pilbara Craton and the Proterozoic Capricorn Orogen (Rudall Province). The basin was deformed and metamorphosed within the Proterozoic Miles and Paterson orogens. Emplacement of mafic intrusions into the basin is constrained to the <950–830 Ma interval (Maidment et al., 2017), which saw extensive juvenile addition into the crust to the east of the Rudall Province at this time. Mafic magmatism of this age also overlaps an 835–830 Ma mafic intrusive event documented elsewhere in the Paterson Orogen (Maidment et al., 2017). Early formation of quartz-pyrite veins at Nifty is constrained by hydrothermal apatite to ca 850–800 Ma, similar to the age of 830 Ma mafic intrusions emplaced during basin extension (Maidment et al., 2017). Mafic magmatism occurred before regional deformation involving east-northeast – west-southwest-directed shortening and was possibly coeval with regional metamorphism. The Keene Basalt in the northwest Officer Basin and its intrusive equivalents in the Pilbara Craton likely also reflect expressions of this extensional process (Haines et al., 2004; Zi et al., 2019). Inversion of the basin by southwest verging thrusting and associated dextral strike-slip faulting took place during the Miles Orogeny at between ca 830 and 650 Ma. A range of granites in the Paterson Orogen have yielded ages of ca 650–630 Ma including rocks at the Venus prospect (Bagas, 2004; Quentin de Gromard et al., 2019). We date a second hydrothermal stage and Cu bearing veins at Nifty to around this age by monazite, consistent with the mobilisation of crustal fluids at this time. More generally, Au–Cu and W mineralisation appears associated with 650–610 Ma intrusions such as the Mount Crofton Suite (Goellnicht et al., 1991) and widespread emplacement of granite in the Percival Lake Province, a Proterozoic Terrane rooted on ca 1950 Ma oceanic crust that lies to the east of the Rudall Province (Lu et al., 2022), which conversely is built on Archean Pilbara Craton substrate. The most conservative interpretation of magmatism, which led to crustal fluids and mineralisation at ca 670–640 and 550–510 Ma at Nifty, is its production during the intracratonic Paterson orogeny, in which pre-existing crust was extensively reworked (Cawood and Korsch, 2008; Maidment et al., 2017).

6. Conclusion

The petrographic observations and in situ apatite and monazite U–Pb–trace element and data presented in this study reveal a minimum of three distinct hydrothermal events in the Nifty Cu deposit in situ, shedding light on the evolution of one of the most prominent, yet cryptic, Cu deposits in Western Australia. Hydrothermal apatite associated with euhedral vein-hosted Py_1 defines the first known hydrothermal event at early-mid Tonian (ca 810 Ma), which variably reset the U–Pb isotope system in pre-existing apatite grains in the host-rock matrix. This first stage is temporally linked to the emplacement of mafic intrusions at 835–830 Ma in the Paterson Orogen. Monazite grains crystallized in interfacial cracks between the vein and host-rock matrix, and in discrete monazite-chalcopyrite veinlets within the matrix, define a later hydrothermal stage at ca 670–640 Ma and 550–510 Ma. Intragranular fluid flow during these Ediacaran–Cambrian events generated Py_1-Py_2 replacement textures, and likely chemically modified the apatite from older quartz-bearing veins leading to dispersion in apparent U–Pb ages spanning 810–640 Ma interval as bracketed by the first generation of apatite and late-stage monazite ages. This 670–640 Ma hydrothermal event is temporally linked with ca 650–630 Ma granitic magmatism in the Paterson Orogen associated with regional Au-Cu mineralization, whereas the later 550–510 Ma event may be associated to intracontinental reactivation of the Paterson Orogen. Ore-textures preserved in the Nifty Cu deposits are highly diachronous, separated by an interval of almost 200 million years. This work highlights the importance of applying in situ geochronological and geochemical tools to unravel discrete mineralisation and/or fluid flow events in regions with long-lived geological histories.

CRediT authorship contribution statement

Bruno V. Ribeiro: Conceptualization, Formal analysis, Investigation, Writing – original draft. **Christopher L. Kirkland:** Conceptualization, Investigation, Resources, Writing – review & editing. **Michael I. H. Hartnady:** Conceptualization, Investigation, Writing – review & editing. **Erin L. Martin:** Validation, Writing – review & editing. **Emily West:** Resources. **Paul Polito:** Resources.

Declaration of Competing Interest

The authors declare that they have no known competing financial interests or personal relationships that could have appeared to influence the work reported in this paper.

Data availability

Data is available in the supplementary materials associated to this paper.

Acknowledgements

This study was supported by the Timescales of Mineral Systems Group (Curtin University) and IGO Ltd. Kai Rankenburg and Bradley McDonald are thanked for assistance during data collection. GeoHistory Facility in the John de Laeter Centre instruments are supported by the Research Office, Curtin University, AuScope (auscope.org.au) and the Australian Government via the National Collaborative Research Infrastructure Strategy (NCRIS). Part of this research was undertaken using the Tescan Clara FESEM (ARC LE190100176) at the John de Laeter

Centre, Curtin University. We sincerely thank Editor Wilson Teixeira and Associate Editor Martin Whitehouse for handling our manuscript, and appreciate the comments by Dr. Chris Mark and an anonymous reviewer, which have benefited this work.

Appendix A. Supplementary material

Supplementary data to this article can be found online at https://doi.org/10.1016/j.precamres.2023.107018.

References

Anderson, B.R., Gemmell, J.B., Berry, R.F., 2001. The Geology of the Nifty Copper Deposit, Throssell Group, Western Australia: implications for Ore Genesis. Econ. Geol. 96, 1535–1565. https://doi.org/10.2113/gsecongeo.96.7.1535.

Anderson, B.R., Gemmell, J.B., Nelson, D.R., 2002. Lead isotope evolution of mineral deposits in the Proterozoic Throssell Group, Western Australia. Econ. Geol. 97, 897–911. https://doi.org/10.2113/gsecongeo.97.4.897.

Anenburg, M., 2020. Rare earth mineral diversity controlled by REE pattern shapes. Mineral Mag. 84, 629–639. https://doi.org/10.1180/mgm.2020.70.

Anenburg, M., Williams, M.J., 2022. Quantifying the tetrad effect, shape components, and Ce–Eu–Gd anomalies in rare earth element patterns. Math. Geosci. 54, 47–70. https://doi.org/10.1007/s11004-021-09959-5.

Bagas, L., 2004. Proterozoic evolution and tectonic setting of the northwest Paterson Orogen, Western Australia. Precambrian Res. 128, 475–496. https://doi.org/10.1016/j.precamres.2003.09.011.

Bagas, L., Smithies, R.H., 1998. Geology of the Connaughton 1:100,000 sheet: 1:100,000. Geological Series Explanatory Notes, Perth.

Barfod, G.H., Krogstad, E.J., Frei, R., Albarède, F., 2005. Lu-Hf and PbSL geochronology of apatites from Proterozoic terranes: a first look at Lu-Hf isotopic closure in metamorphic apatite. Geochim. Cosmochim. Acta 69, 1847–1859. https://doi.org/10.1016/j.gca.2004.09.014.

Belousova, E.A., Walters, S., Griffin, W.L., O'Reilly, S.Y., 2001. Trace-element signatures of apatites in granitoids from the Mt Isa Inlier, Northwestern Queensland. Aust. J. Earth Sci. 48, 603–619. https://doi.org/10.1046/j.1440-0952.2001.00879.x.

Belousova, E.A., Griffin, W.L., O'Reilly, S.Y., Fisher, N.I., 2002. Apatite as an indicator mineral for mineral exploration: trace-element compositions and their relationship to host rock type. J. Geochem. Explor. 76, 45–69.

Betts, P.G., Armit, R.J., Stewart, J., Aitken, A.R.A., Ailleres, L., Donchak, P., Hutton, L., Withnall, I., Giles, D., 2015. Supercontinent cycles through Earth history. Geol. Soc. Lond. Spec. Publ. 424, 47–81.

Brugger, J., Etschmann, B., Pownceby, M., Liu, W., Grundler, P., Brewe, D., 2008. Oxidation state of europium in scheelite: tracking fluid–rock interaction in gold deposits. Chem Geol 257, 26–33. https://doi.org/10.1016/j.chemgeo.2008.08.003.

Cabrita, D.I.G., Faleiros, F.M., Ribeiro, B.v., Menegon, L., Cawood, P.A., Campanha, G.A.C., 2022. Deformation, thermochronology and tectonic significance of the crustal-scale Cubatão Shear Zone, Ribeira Belt, Brazil. Tectonophysics 229278. https://doi.org/10.1016/j.tecto.2022.229278.

Cao, M., Li, G., Qin, K., Seitmuratova, E.Y., Liu, Y., 2012. Major and trace element characteristics of apatites in granitoids from central Kazakhstan: implications for petrogenesis and mineralization. Resour. Geol. 62, 63–83. https://doi.org/10.1111/j.1751-3928.2011.00180.x.

Cawood, P.A., Korsch, R.J., 2008. Assembling Australia: proterozoic building of a continent. Precambrian Res. 166, 1–35. https://doi.org/10.1016/j.precamres.2008.08.006.

Chen, M., Bagas, L., Liao, X., Zhang, Z., Li, Q., 2019. Hydrothermal apatite SIMS Th Pb dating: constraints on the timing of low-temperature hydrothermal Au deposits in Nibao, SW China. Lithos 324–325, 418–428. https://doi.org/10.1016/j.lithos.2018.11.018.

Chew, D.M., Petrus, J.A., Kamber, B.S., 2014. U-Pb LA-ICPMS dating using accessory mineral standards with variable common Pb. Chem. Geol. 363, 185–199. https://doi.org/10.1016/j.chemgeo.2013.11.006.

Chew, D.M., Babechuk, M.G., Cogné, N., Mark, C., O'Sullivan, G.J., Henrichs, I.A., Doepke, D., McKenna, C.A., 2016. (LA, Q)-ICPMS trace-element analyses of Durango and McClure Mountain apatite and implications for making natural LA-ICPMS mineral standards. Chem. Geol. 435, 35–48. https://doi.org/10.1016/j.chemgeo.2016.03.028.

Chew, D.M., Spikings, R.A., 2015. Geochronology and thermochronology using apatite: time and temperature, lower crust to surface. Elements 11, 189–194. https://doi.org/10.2113/gselements.11.3.189.

Chew, D.M., Sylvester, P.J., Tubrett, M.N., 2011. U-Pb and Th-Pb dating of apatite by LA-ICPMS. Chem. Geol. 280, 200–216. https://doi.org/10.1016/j.chemgeo.2010.11.010.

Chu, M., Wang, K., Griffin, W.L., Chung, S., Reilly, S.Y.O., Pearson, N.J., Iizuka, Y., 2009. Apatite composition: tracing petrogenetic processes in Transhimalayan granitoids. J. Petrol. 50, 1829–1855. https://doi.org/10.1093/petrology/egp054.

Clarke, G.L., 1991. Proterozoic tectonic reworking in the Rudall complex, Western Australia. Aust. J. Earth Sci. 38, 31–44. https://doi.org/10.1080/08120099108727953.

Corfu, F., Stone, D., 1998. The significance of titanite and apatite U-Pb ages: constraints for the post-magmatic thermal-hydrothermal evolution of a batholithic complex, Berens River area, northwestern Superior Province, Canada. Geochim. Cosmochim. Acta 62, 2979–2995. https://doi.org/10.1016/S0016-7037(98)00225-7.

Cox, S.F., 1987. Antitaxial crack-seal vein microstructures and their relationship to displacement paths. J. Struct. Geol. 9, 779–787. https://doi.org/10.1016/0191-8141(87)90079-4.

de Melo, G.H.C., Monteiro, L.V.S., Xavier, R.P., Moreto, C.P.N., Arquaz, R.M., Silva, M.A.D., 2019. Evolution of the Igarapé Bahia Cu-Au deposit, Carajás Province (Brazil): early syngenetic chalcopyrite overprinted by IOCG mineralization. Ore Geol. Rev. 111, 102993 https://doi.org/10.1016/j.oregeorev.2019.102993.

Dempster, T.J., Jolivet, M., Tubrett, M.N., Braithwaite, C.J.R., 2003. Magmatic zoning in apatite: a monitor of porosity and permeability change in granites. Contrib. Miner. Petrol. 145, 568–577. https://doi.org/10.1007/s00410-003-0471-0.

Durocher, K.E., Kyser, T.K., Marlatt, J., Hanly, A., 2003. New $^{40}Ar/^{39}Ar$ ages from the central Paterson Orogen, Western Australia. Aust. J. Earth Sci. 50, 601–610. https://doi.org/10.1046/j.1440-0952.2003.01011.x.

Duuring, P., Guilliamse, J.N., Kelsey, D.E., Fielding, I.O.H., Fonteneau, L., 2022. Alteration and Cu-Au mineralization at the Obelisk Prospect, Paterson Orogen, Western Australia. Perth, Western Australia.

Engi, M., 2018. Petrochronology based on REE-minerals: monazite, allanite, xenotime, apatite. Rev. Mineral Geochem. 83, 365–418. https://doi.org/10.2138/rmg.2017.83.12.

Faleiros, F.M., Ribeiro, B.v., Campanha, G.A.C., Cawood, P.A., Cabrita, D.I.G., Yogi, M.T.A.G., Milani, L.A., Lemos-Santos, D.v., Almeida, V.v., Rodrigues, S.W.O., Malta, I.S., Forero-Ortega, A.J., 2022. Strain partitioning along terrane bounding and intraterrane shear zones: constraints from a long-lived transpressional system in West Gondwana (Ribeira Belt, Brazil). Lithosphere 2022. https://doi.org/10.2113/2022/2103213.

Ferguson, K.M., Bagas, L., Ruddock, I., 2005. Mineral Occurrences and Exploration Potential of the Paterson Area, Perth.

Gardiner, N.J., Maidment, D.W., Kirkland, C.L., Bodorkos, S., Smithies, R.H., Jeon, H., 2018. Isotopic insight into the Proterozoic crustal evolution of the Rudall Province, Western Australia. Precambrian Res. 313, 31–50. https://doi.org/10.1016/j.precamres.2018.05.003.

Goellnicht, N.M., Groves, D.I., McNaughton, N.J., 1991. Late proterozoic fractionated granitoids of the mineralized Telfer area, Paterson province, Western Australia. Precambrian Res. 51, 375–391. https://doi.org/10.1016/0301-9268(91)90109-N.

Haines, P.W., Mory, A.J., Stevens, M.K., Ghori, K.A.R., 2004. GSWA Lancer 1 Well Completion Report (basic data) Officer and Gunbarrel Basins, Western Australia.

Harlov, D.E., 2015. Apatite: a fingerprint for metasomatic processes. Elements 11, 171–176. https://doi.org/10.2113/gselements.11.3.171.

Horstwood, M.S.A., Košler, J., Gehrels, G., Jackson, S.E., McLean, N.M., Paton, C., Pearson, N.J., Sircombe, K., Sylvester, P., Vermeesch, P., Bowring, J.F., Condon, D.J., Schoene, B., 2016. Community-Derived Standards for LA-ICP-MS U-(Th-)Pb Geochronology – Uncertainty Propagation, Age Interpretation and Data Reporting. Geostandards and Geoanalytical Research 40 (3), 311–332. https://doi.org/10.1111/j.1751-908X.2016.00379.x.

Henrichs, I.A., O'Sullivan, G., Chew, D.M., Mark, C., Babechuk, M.G., McKenna, C., Emo, R., 2018. The trace element and U-Pb systematics of metamorphic apatite. Chem. Geol. 483, 218–238. https://doi.org/10.1016/j.chemgeo.2017.12.031.

Henrichs, I.A., Chew, D.M., O'Sullivan, G.J., Mark, C., McKenna, C., Guyett, P., 2019. Trace element (Mn-Sr-Y-Th-REE) and U-Pb isotope systematics of metapelitic apatite during progressive greenschist- to amphibolite-facies Barrovian metamorphism.pdf. Geochem. Geophys. Geosyst. 20, 4103–4129. https://doi.org/10.1029/2019GC008359.

Hetherington, C.J., Harlov, D.E., Budzyń, B., 2010. Experimental metasomatism of monazite and xenotime: mineral stability, REE mobility and fluid composition. Mineral. Petrol. 99, 165–184. https://doi.org/10.1007/s00710-010-0110-1.

Hickman, A.H., Clarke, G.L., 1994. Geology of the Broadhurst 1:100 000 sheet: Explanatory Notes, Perth.

Hickman, A., Bagas, L., 1999. Geological evolution of the Palaeoproterozoic Talbot Terrane and adjacent Meso- and Neoproterozoic successions, Paterson Orogen. Western Australia, Perth.

Hrstka, T., Gottlieb, P., Skála, R., Breiter, K., Motl, D., 2018. Automated mineralogy and petrology - applications of TESCAN Integrated Mineral Analyzer (TIMA). J. Geosci. 47–63 https://doi.org/10.3190/jgeosci.250.

Huston, D.L., Maas, R., Czarnota, K., 2020. The age, metal source and genesis of the Nifty copper deposit in the context of the geological evolution of the Paterson Province, Western Australia. Miner. Depos. 55, 147–162. https://doi.org/10.1007/s00126-019-00881-9.

Kirkland, C.L., Yakymchuk, C., Szilas, K., Evans, N., Hollis, J., McDonald, B., Gardiner, N.J., 2018. Apatite: a U-Pb thermochronometer or geochronometer? Lithos 318–319, 143–157. https://doi.org/10.1016/j.lithos.2018.08.007.

Krneta, S., Ciobanu, C.L., Cook, N.J., Ehrig, K., Kontonikas-Charos, A., 2017. Rare earth element behaviour in apatite from the olympic dam Cu–U–Au–Ag deposit, South Australia. Minerals 7, 135. https://doi.org/10.3390/min7080135.

Krneta, S., Ciobanu, C., Cook, N., Ehrig, K., 2018. Numerical modeling of REE fractionation patterns in fluorapatite from the olympic dam deposit (South Australia). Minerals 8, 342. https://doi.org/10.3390/min8080342.

Larson, K.P., Shrestha, S., Cottle, J.M., Guilmette, C., Johnson, T.A., Gibson, H.D., Gervais, F., 2022. Re-evaluating monazite as a record of metamorphic reactions. Geosci. Front. 13, 101340 https://doi.org/10.1016/j.gsf.2021.101340.

Long, X.-Y., Tang, J., Xu, W.-L., Sun, C.-Y., Luan, J.-P., Xiong, S., Zhang, X.-M., 2023. Trace element and Nd isotope analyses of apatite in granitoids and metamorphosed granitoids from the eastern Central Asian Orogenic Belt: Implications for petrogenesis and post-magmatic alteration. Geosci. Front. 14, 101517 https://doi.org/10.1016/j.gsf.2022.101517.

Lu, Y., Wingate, M.T.D., Smithies, R.H., Gessner, K., Johnson, S.P., Kemp, A.I.S., Kelsey, D.E., Haines, P.W., Martin, D.M., Martin, L., Lindsay, M., 2022. Preserved intercratonic lithosphere reveals Proterozoic assembly of Australia. Geology 50, 1202–1207. https://doi.org/10.1130/G50256.1.

Ludwig, K.R., 1991. Isoplot–a plotting and regression program for radiogenic isotope data. USGS Open-file report 91–445.

Maidment, D.W., Huston, D.L., Beardsmore, T., 2017. Paterson Orogen geology and metallogeny. In: Phillips, G.N. (Ed.), Australian Ore Deposits, pp. 411–416.

Mao, M., Rukhlov, A.S., Rowins, S.M., Spence, J., Coogan, L.A., 2016. Apatite trace element compositions: a robust new tool for mineral exploration. Econ. Geol. 111, 1187–1222. https://doi.org/10.2113/econgeo.111.5.1187.

Martin, E.L., Collins, W.J., Kirkland, C.L., 2017. An Australian source for Pacific-Gondwanan zircons: Implications for the assembly of northeastern Gondwana. Geology G39152, 1. https://doi.org/10.1130/G39152.1.

Mcarthur, J.M., 1985. Francolite geochemistry—compositional controls during formation, diagenesis, metamorphism and weathering. Geochim. Cosmochim. Acta 49, 23–35. https://doi.org/10.1016/0016-7037(85)90188-7.

McDonough, W.F., Sun, S.-s., 1995. The composition of the Earth. Chem. Geol. 2541, 223–253.

Miles, A.J., Graham, C.M., Hawkesworth, C.J., Gillespie, M.R., Hinton, R.W., Bromiley, G.D., 2014. Apatite: a new redox proxy for silicic magmas? Geochim. Cosmochim. Acta 132, 101–119. https://doi.org/10.1016/j.gca.2014.01.040.

Milton, J.E., Hickey, K.A., Gleeson, S.A., Falck, H., Allaz, J., 2017. In situ monazite dating of sediment-hosted stratiform copper mineralization in the redstone copper belt, Northwest Territories, Canada: cupriferous fluid flow late in the evolution of a Neoproterozoic sedimentary basin. Econ. Geol. 112, 1773–1806. https://doi.org/10.5382/econgeo.2017.4529.

Myers, J.S., Shaw, R.D., Tyler, I.M., 1996. Tectonic evolution of Proterozoic Australia. Tectonics 15, 1431–1446. https://doi.org/10.1029/96TC02356.

Nelson, D.R., 2002. Compilation of Geochronology Data, Perth.

O'Neill, H.S.C., 2016. The smoothness and shapes of chondrite-normalized rare earth element patterns in basalts. J. Petrol. 57, 1463–1508. https://doi.org/10.1093/petrology/egw047.

O'Sullivan, G., Chew, D., Kenny, G., Henrichs, I., Mulligan, D., 2020. The trace element composition of apatite and its application to detrital provenance studies. Earth Sci. Rev. 201, 103044 https://doi.org/10.1016/j.earscirev.2019.103044.

Odlum, M.L., Stockli, D.F., 2020. Geochronologic constraints on deformation and metasomatism along an exhumed mylonitic shear zone using apatite U-Pb, geochemistry, and microtextural analysis. Earth Planet Sci. Lett. 538, 116177 https://doi.org/10.1016/j.epsl.2020.116177.

Odlum, M.L., Levy, D.A., Stockli, D.F., Stockli, L.D., DesOrmeau, J.W., 2022. Deformation and metasomatism recorded by single-grain apatite petrochronology. Geology. https://doi.org/10.1130/G49809.1.

Pan, L.C., Hu, R.Z., Wang, X.S., Bi, X.W., Zhu, J.J., Li, C., 2016. Apatite trace element and halogen compositions as petrogenetic-metallogenic indicators: examples from four granite plutons in the Sanjiang region, SW China. Lithos 254–255, 118–130. https://doi.org/10.1016/j.lithos.2016.03.010.

Paton, C., Hellstrom, J., Paul, B., Woodhead, J., Hergt, J., 2011. Iolite: freeware for the visualisation and processing of mass spectrometric data. J. Anal. At. Spectrom. 26, 2508. https://doi.org/10.1039/c1ja10172b.

Payne, J.L., Morrissey, L.J., Tucker, N.M., Roche, L.K., Szpunar, M.A., Neroni, R., 2021. Granites and gabbros at the dawn of a coherent Australian continent. Precambrian Res. 359, 106189 https://doi.org/10.1016/j.precamres.2021.106189.

Piccoli, P.M., Candela, P.A., 2019. Apatite in igneous systems. Phosphates: Geochem., Geobiol. Mater. Import. 48, 255–292. https://doi.org/10.2138/rmg.2002.48.6.

Poitrasson, F., Chenery, S., Bland, D.J., 1996. Contrasted monazite hydrothermal alteration mechanisms and their geochemical implications. Earth Planet Sci. Lett. 145, 79–96. https://doi.org/10.1016/S0012-821X(96)00193-8.

Prent, A.M., Beinlich, A., Raimondo, T., Kirkland, C.L., Evans, N.J., Putnis, A., 2020. Apatite and monazite: an effective duo to unravel superimposed fluid-flow and deformation events in reactivated shear zones. Lithos 376–377, 105752. https://doi.org/10.1016/j.lithos.2020.105752.

Quentin de Gromard, R., Kirkland, C.L., Howard, H.M., Wingate, M.T.D., Jourdan, F., McInnes, B.I.A., Danišík, M., Evans, N.J., McDonald, B.J., Smithies, R.H., 2019. When will it end? Long-lived intracontinental reactivation in central Australia. Geosci. Front. 10, 149–164. https://doi.org/10.1016/j.gsf.2018.09.003.

Reed, M.H., 2006. Sulfide mineral precipitation from hydrothermal fluids. Rev. Mineral Geochem. 61, 609–631. https://doi.org/10.2138/rmg.2006.61.11.

Ribeiro, B.V., Lagoeiro, L., Faleiros, F.M., Hunter, N.J.R., Queiroga, G., Raveggi, M., Cawood, P.A., Finch, M., Campanha, G.A.C., 2020a. Strain localization and fluid-assisted deformation in apatite and its influence on trace elements and U-Pb systematics. Earth Planet Sci. Lett. 545, 116421 https://doi.org/10.1016/j.epsl.2020.116421.

Ribeiro, B.V., Mulder, J.A., Faleiros, F.M., Kirkland, C.L., Cawood, P.A., O'Sullivan, G., Campanha, G.A.C., Finch, M.A., Weinberg, R.F., Nebel, O., 2020b. Using apatite to resolve the age and protoliths of mid-crustal shear zones: a case study from the Taxaquara Shear Zone. SE Brazil. Lithos 378–379, 105817. https://doi.org/10.1016/j.lithos.2020.105817.

Ribeiro, B.V., Finch, M.A., Cawood, P.A., Faleiros, F.M., Murphy, T.D., Simpson, A., Glorie, S., Tedeschi, M., Armit, R., Barrote, V.R., 2022. From microanalysis to supercontinents: insights from the Rio Apa Terrane into the Mesoproterozoic SW Amazonian Craton evolution during Rodinia assembly. J. Metam. Geol. 40, 631–663. https://doi.org/10.1111/jmg.12641.

Sawlowicz, Z., 1993. Pyrite framboids and their development: a new conceptual mechanism. Geol. Rundsch. 82, 148–156. https://doi.org/10.1007/BF00563277.

Schmitz, M.D., Bowring, S.A., Ireland, T.R., 2003. Evaluation of Duluth Complex anorthositic series (AS3) zircon as a U-Pb geochronological standard: new high-precision isotope dilution thermal ionization mass spectrometry results. Geochim. Cosmochim. Acta 67, 3665–3672. https://doi.org/10.1016/S0016-7037(03)00200-X.

Schoene, B., Bowring, S.A., 2006. U-Pb systematics of the McClure Mountain syenite: thermochronological constraints on the age of the 40Ar/39Ar standard MMhb. Contrib. Miner. Petrol. 151, 615–630. https://doi.org/10.1007/s00410-006-0077-4.

Smithies, R.H., Bagas, L., 1997. High pressure amphibolite-granulite facies metamorphism in the Paleoproterozoic Rudall Complex, central Western Australia. Precambrian Res. 83, 243–265. https://doi.org/10.1016/S0301-9268(96)00051-4.

Spear, F.S., Pyle, J.M., 2019. Apatite, monazite, and xenotime in metamorphic rocks. Phosphates: Geochem.Geobiol. Mater. Import. 48, 293–336. https://doi.org/10.2138/rmg. 2002.48.7.

Stacey, J.S., Kramers, J.D., 1975. Approximation of terrestrial lead isotope evolution by a two-stage model. Earth Planet Sci. Lett. 26, 207–221. https://doi.org/10.1016/0012-821X(75)90088-6.

Thompson, J., Meffre, S., Maas, R., Kamenetsky, V., Kamenetsky, M., Goemann, K., Ehrig, K., Danyushevsky, L., 2016. Matrix effects in Pb/U measurements during LA-ICP-MS analysis of the mineral apatite. J. Anal. At. Spectrom. 31, 1206–1215. https://doi.org/10.1039/C6JA00048G.

Thomson, S.N., Gehrels, G.E., Ruiz, J., Buchwaldt, R., 2012. Routine low-damage apatite U-Pb dating using laser ablation–multicollector–ICPMS. Geochem. Geophys, Geosyst 13.

Tomascak, P.B., Krogstad, E.J., Walker, R.J., 1996. U-Pb Monazite Geochronology of Granitic Rocks from Maine: Implications for Late Paleozoic Tectonics in the Northern Appalachians. The Journal of Geology 104 (2), 185–195. https://doi.org/10.1086/629813.

van Daele, J., Dewaele, S., Melcher, F., Onuk, P., Spikings, R., Glorie, S., Jepson, G., Muchez, P., 2020. Geochronology of metamorphism, deformation and fluid circulation: a comparison between and Ar-Ar phyllosilicate and U-Pb apatite systematics in the Karagwe-Ankole Belt (Central Africa). Gondw. Res. 83, 279–297. https://doi.org/10.1016/j.gr.2020.02.008.

Vermeesch, P., 2018. IsoplotR: a free and open toolbox for geochronology. Geosci. Front. 9, 1479–1493. https://doi.org/10.1016/j.gsf.2018.04.001.

Watson, E.B., Green, T.H., 1981. Apatite/liquid partition coefficients for the rare earth elements and strontium. Earth Planet Sci. Lett. 56, 405–421. https://doi.org/10.1016/0012-821X(81)90144-8.

Weinberg, R.F., Wolfram, L.C., Nebel, O., Hasalová, P., Závada, P., Kylander-Clark, A.R.C., Becchio, R., 2020. Decoupled U-Pb date and chemical zonation of monazite in migmatites: the case for disturbance of isotopic systematics by coupled dissolution-reprecipitation. Geochim. Cosmochim. Acta 269, 398–412. https://doi.org/10.1016/j.gca.2019.10.024.

Whitney, D.L., Evans, B.W., 2010. Abbreviations for names of rock-forming minerals. Am. Mineral. 95, 185–187. https://doi.org/10.2138/am.2010.3371.

Williams, I.R., Bagas, L., 1999. Geology of the Throssell 1:100 000 sheet, Perth.

Williams, I.R., Myers, J.S., 1990. Paterson Orogen. In: Geology and Mineral Resources of Western Australia, Memoir 3. Perth.

Williams, M.L., Jercinovic, M.J., Harlov, D.E., Budzyń, B., Hetherington, C.J., 2011. Resetting monazite ages during fluid-related alteration. Chem. Geol. 283, 218–225. https://doi.org/10.1016/j.chemgeo.2011.01.019.

Yang, Y.-H., Wu, F.-Y., Yang, J.-H., Chew, D.M., Xie, L.-W., Chu, Z.-Y., Zhang, Y.-B., Huang, C., 2014. Sr and Nd isotopic compositions of apatite reference materials used in U–Th–Pb geochronology. Chem. Geol. 385, 35–55. https://doi.org/10.1016/j.chemgeo.2014.07.012.

Zafar, T., Rehman, H.U., Mahar, M.A., Alam, M., Oyebamiji, A., Rehman, S.U., Leng, C. B., 2020. A critical review on petrogenetic, metallogenic and geodynamic implications of granitic rocks exposed in north and east China: new insights from apatite geochemistry. J Geodyn 136. https://doi.org/10.1016/j.jog.2020.101723.

Zhong, R., Brugger, J., Chen, Y., Li, W., 2015. Contrasting regimes of Cu, Zn and Pb transport in ore-forming hydrothermal fluids. Chem. Geol. 395, 154–164. https://doi.org/10.1016/j.chemgeo.2014.12.008.

Zhu, X.K., O'Nions, R.K., 1999. Monazite chemical composition: some implications for monazite geochronology. Contrib. Miner. Petrol. 137, 351–363. https://doi.org/10.1007/s004100050555.

Zi, J., Haines, P.W., Wang, X., Jourdan, F., Rasmussen, B., Halverson, G.P., Sheppard, S., Li, C., 2019. Pyroxene ^{40} Ar/ ^{39} Ar dating of basalt and applications to large igneous provinces and Precambrian stratigraphic correlations. J. Geophys. Res. Solid Earth 124, 8313–8330. https://doi.org/10.1029/2019JB017713.